

Challenges to the Two-Infall Scenario by Large Stellar Age Catalogs

LIAM O. DUBAY^{1,2}, JENNIFER A. JOHNSON^{1,2}, JAMES W. JOHNSON³, JOHN D. ROBERTS^{1,2} AND COAUTHORS

¹*Department of Astronomy, The Ohio State University, 140 W. 18th Ave, Columbus OH 43210, USA*

²*Center for Cosmology and AstroParticle Physics, The Ohio State University, 191 W. Woodruff Ave., Columbus OH 43210, USA*

³*Observatories of the Carnegie Institution for Science, 813 Santa Barbara St., Pasadena CA 91101, USA*

ABSTRACT

The Milky Way stellar disk is composed of two chemically distinct populations that are separated by their $[\alpha/\text{Fe}]$ ratios. This α -bimodality is not a universal feature of simulated disk galaxies and may point to the Milky Way’s unique evolutionary history. A popular explanation is the two-infall scenario, which postulates that two periods of substantial accretion rates dominate the assembly history of the Galaxy. However, most previous studies using the two-infall scenario have explored a limited portion of the parameter space, typically neglecting radial migration and assuming that the Galactic disk never ejected a substantial outflow. Thanks to advances in stellar age measurements in recent years, we can now also compare this popular model to more direct measurements of the Galaxy’s evolutionary timescales across the disk from large stellar catalogs. We run multi-zone galactic chemical evolution (GCE) models with a two-infall-driven star formation history, radially dependent mass-loaded outflows, and a prescription for radial migration tuned to a hydrodynamical simulation. We compare our model results to abundance patterns across the disk from APOGEE DR17, supplemented with stellar age estimates through multiple methods. Although the two-infall scenario offers a natural explanation for the $[\alpha/\text{Fe}]$ bimodality, it struggles to explain several features of the age–abundance structure in the disk. The two-infall scenario generically predicts a massive and long-lasting dilution event, but the data show that stellar metallicity is remarkably constant with age across much of the Galactic disk. This apparent age-independence places considerable restrictions upon the two-infall parameter space. These issues can be mitigated, but not completely resolved, by allowing the accreted gas to be pre-enriched to low metallicity. **Add a sentence about larger implications for merger-dominated SFHs. Also, mention LMR age patterns?**

1. INTRODUCTION

GALACTIC CHEMICAL EVOLUTION (GCE) studies aim to explain the observed stellar abundance patterns in the Milky Way (MW) by modeling the star formation history and evolution of the Galaxy. A long-standing paradigm of GCE is that the metallicity of the interstellar medium (ISM) increases over time due to supernova enrichment from successive generations of stars (e.g., Tinsley 1979; Matteucci & Greggio 1986). In this view, one feature of the MW disk that is difficult to explain is the so-called “ α -bimodality”: the presence of two populations of stars at similar metallicity but separated by their $[\alpha/\text{Fe}]$ ratio (e.g., Bensby et al. 2014). The high- α sequence consists of old stars

($\gtrsim 9$ Gyr; e.g., Pinsonneault et al. 2025) with super-Solar $[\alpha/\text{Fe}]$ and is associated with the kinematic thick disk (e.g., Fuhrmann 1998), while the low- α sequence is younger, with approximately Solar $[\alpha/\text{Fe}]$, and is associated with the thin disk. The α -bimodality is present across the Galactic disk, but the relative strength of the high- and low- α sequences varies by location (Hayden et al. 2015).

An explanation for the MW α -bimodality has yet to be broadly accepted in the GCE literature. An α -bimodality is not a universal feature in simulated MW-mass galaxies, and may be rare (e.g., Mackereth et al. 2018; Parul et al. 2025). (citations; also mention external galaxies?), so its presence and characteristics in our Galaxy may provide clues to its unique evolutionary history. GCE models that attempt to solve this problem generally fall into two camps. Some explain the α -bimodality as a result of secular processes, such as the radial migration of stars and the inside-out growth

of the disk (e.g., Kubryk et al. 2015; Sharma et al. 2021; Chen et al. 2023; Prantzos et al. 2023). Others argue for a bursty star formation history, perhaps driven by multiple discrete accretion events (e.g., Chiappini et al. 1997; Mackereth et al. 2018; Spitoni et al. 2023) or a change in the star formation efficiency (e.g. Conroy et al. 2022).

The two-infall model of chemical evolution was proposed by Chiappini et al. (1997) to explain the origin of the high- and low- α disks. Though the model has been revised and refined since, the basic premise remains the same: the rate of gas infall onto the Galaxy is described by two consecutive, exponentially declining bursts. The relatively low infall rate between the two bursts leads to a lower star formation rate, allowing the gas abundance to evolve between the high- and low- α sequences while producing few stars in between. The infall timescale for the low- α disk can be varied to produce inside-out disk growth and a radial metallicity gradient (Romano et al. 2000). The initial model of Chiappini et al. (1997) successfully reproduced the available abundance data at the time, which were largely confined to the Solar neighborhood.

Subsequent studies refined the two-infall model to reproduce abundance data across the disk (e.g., Chiappini et al. 2001, 2003). Others have explored the SN Ia delay-time distribution (Matteucci et al. 2009; Palicio et al. 2023), galactic fountains (Spitoni et al. 2009), radial gas flows (Spitoni & Matteucci 2011; Palla et al. 2020), a variable star formation efficiency (Spitoni & Matteucci 2011; Palla et al. 2020), radial stellar migration (Spitoni et al. 2015; Palla et al. 2022), azimuthal abundance variations due to spiral modes (Spitoni et al. 2019), and pre-enriched gas infall (Palla et al. 2020; Spitoni et al. 2024) in a two-infall context. Recently, Spitoni et al. (2023) and Palla et al. (2024) proposed a third gas accretion event in the last ~ 3 Gyr to match the inferred star formation history from *Gaia* (Ruiz-Lara et al. 2020) and explain the recent abundance evolution of the Solar neighborhood.

Most previous studies of the two-infall model have not included mass-loaded outflows. Some hydrodynamic simulations of Galactic fountains ejected by CC SNe have shown that ejected material falls back onto the disk on relatively short timescales (Spitoni et al. 2008, 2009) and close to their point of origin (Melioli et al. 2008, 2009), suggesting the effect on GCE could be minimal. However, other simulations of MW-like galaxies with different feedback prescriptions do produce mass-loaded outflows (citations). Empirically, mass-loaded outflows have been observed in nearby starburst galaxies (citations) and dwarf galaxies (citations) but not MW-like systems, although the predicted column densities are be-

low current detection limits (citations). In the absence of outflows, some two-infall studies have implemented radial gas flows or a variable star formation efficiency in order to regulate the radial metallicity gradient (Spitoni & Matteucci 2011; Palla et al. 2020).

Discuss yields, degeneracy with outflows and Rodriguez measurements. Emphasize that degeneracy with outflows prohibits direct estimates of yields from GCE. We aim to study the effect of the yield assumptions, which necessitates adjusting the outflows as well.

The two-infall model attempts to reproduce the full distribution of stellar abundances in the Solar neighborhood through a single, continuous evolutionary track. However, the current body of evidence suggests that many of the stars that make up the wings of the local metallicity distribution originate from elsewhere in the Galaxy. Sellwood & Binney (2002) first showed that transient spiral perturbations can induce large changes in the guiding radius of a star without kinematic heating, and it is now understood that the stars that make up the Solar neighborhood are drawn from a wide range of birth radii (e.g., Schönrich & Binney 2009; Frankel et al. 2018; Lehmann et al. 2024). Some studies have attempted to derive stellar birth radii (e.g., Ratcliffe et al. 2023; Lu et al. 2024), though such an endeavor requires also reconstructing the evolution of the Milky Way’s radial metallicity gradient. While the strength and speed of radial migration in the disk are not precisely measured, it is clear that a single chemical evolution track need not explain the entirety of the local observed abundance distribution.

The chemical and kinematic separation of the high- and low- α disks remains the primary observational evidence behind the two-infall model. Spitoni et al. (2024) argued that the observed gap between the sequences in $[\alpha/\text{Fe}]$, contrasted with their overlap in $[\alpha/\text{H}]$, indicates a period of reduced star formation, which is a natural consequence of the two-infall model. In different samples, Nissen et al. (2020) and Nataf et al. (2024) observed multiple sequences in the local age-metallicity relation, which would naturally be explained by the two-infall scenario. Many two-infall studies have also reproduced the metallicity gradient, the local surface densities of stars and gas, and the local star formation and supernova rates (citations), although these observables can also be matched by other models (citations).

In contrast to the two-infall scenario, a number of studies have attempted to explain the α -bimodality through purely secular processes. Using a detailed prescription for radial migration, Schönrich & Binney (2009) produced distinct high- and low- α sequences, but they did not overlap in metallicity space as would be

found by later surveys (e.g., [Bensby et al. 2014](#)). Others have produced a more MW-like α -bimodality using a combination of radial migration and inside-out galaxy growth (e.g., [Kubryk et al. 2015](#); [Sharma et al. 2021](#); [Chen et al. 2023](#); [Prantzos et al. 2023](#)). In this scenario, the local high- α population originates from the inner Galaxy, where the star formation rate peaked early in its history. [Sharma et al. \(2021\)](#) and [Chen et al. \(2023\)](#) suggest that a simultaneous decline in the star formation rate and the $[\alpha/\text{Fe}]$ ratio is needed to separate the sequences in chemical space. [Chen & Prantzos \(2025\)](#) additionally argue that the double sequence in the local age-metallicity relation observed by [Nissen et al. \(2020\)](#) can also be explained by smooth star formation with inside-out growth. On the other hand, some GCE models that incorporate both radial migration and smooth, inside-out star formation have failed to produce an α -bimodality (e.g., [Johnson et al. 2021](#); [Dubay et al. 2024](#)). While the α -bimodality remains a key piece of evidence for the two-infall scenario, it has been reproduced by other models.

As stellar age estimation techniques have improved over recent years, large catalogs have become available with ages for hundreds of thousands or even millions of stars from a wide swath of the Galaxy. In a challenge to the traditional view of GCE, which expects the ISM metallicity to continually increase over time, [Johnson et al. \(2024\)](#) examined the age-metallicity relation at different radii from the astroNN catalog ([Mackereth et al. 2019](#)) and found that the mode of the metallicity distribution at a given radius is nearly independent from age over the past ~ 9 Gyr. They propose an “equilibrium scenario” in which the local metallicity is driven by the ratio of star formation to accretion at a given radius, which evolves to a constant over \sim Gyr timescales. Whether the equilibrium metallicity is regulated by outflows, as proposed by [Johnson et al. \(2024\)](#), or by other factors such as a radial gas flow, the current data suggest that the gas abundance across the Galaxy has evolved very little over most of the thin disk lifetime.

In light of the findings of [Johnson et al. \(2024\)](#) and a new empirical yield scale from [Weinberg et al. \(2024\)](#), we evaluate the predictions of the two-infall model against stellar age and abundance data across the MW disk. We run multi-zone GCE models with a two-infall accretion history, radially-dependent mass-loaded outflows, and a prescription for radial migration tuned to a hydrodynamical simulation. We investigate the impact of the scale of SN yields and outflows, the strength of radial migration, the enrichment of the circumgalactic medium, and the local disk mass surface density ratio on the GCE model predictions. We compare our results to

abundance distributions across the disk from APOGEE DR17, and to age-abundance relations from multiple age catalogs. We describe our observational sample in Section 2, and we detail our chemical evolution models and parameter selection in Section 3. We compare our multi-zone model predictions to the data in Section 4. We discuss in Section 5 and conclude in Section 6.

2. OBSERVATIONAL SAMPLE

We compare our models against stellar abundances from the Apache Point Observatory Galactic Evolution Experiment (APOGEE; [Majewski et al. 2017](#)) data release 17 (DR17; [Abdurro’uf et al. 2022](#)). APOGEE data were obtained from infrared spectrographs ([Wilson et al. 2019](#)) mounted on the 2.5-meter Sloan Foundation Telescope ([Gunn et al. 2006](#)) at Apache Point Observatory and the Irénée DuPont Telescope ([Bowen & Vaughan 1973](#)) at Las Campanas Observatory. The data reduction pipeline is described by [Nidever et al. \(2015\)](#), and APOGEE Stellar Parameter and Chemical Abundance Pipeline (ASPCAP) is detailed by [Holtzman et al. \(2015\)](#), [García Pérez et al. \(2016\)](#), and [Jönsson et al. \(2020\)](#).

We obtain a sample of 171 635 red giant branch and red clump stars with high-quality spectra using the selection criteria listed in Table 1, which are adapted from [Hayden et al. \(2015\)](#). Table 2 presents the median statistical uncertainty and uncertainty dispersion ($95^{\text{th}} - 5^{\text{th}}$ percentile difference) of the calibrated $[\text{Fe}/\text{H}]$ and $[\text{O}/\text{Fe}]$ abundances for our sample. When calculating the galactocentric radius R_{gal} and midplane distance z of each star, we use the [Bailer-Jones et al. \(2021\)](#) photogeometric distance estimates from *Gaia* Early Data Release 3 ([Gaia Collaboration et al. 2016, 2021](#)) included in the APOGEE DR17 catalog and we adopt the Galactic coordinates of the Sun $(R, z)_{\odot} = (8.122, 0.0208)$ kpc ([GRAVITY Collaboration et al. 2018](#); [Bennett & Bovy 2019](#)). Table 3 presents the number of APOGEE stars in bins of R_{gal} and $|z|$; typical distance uncertainties are much smaller than the bin width (do I need this table?).

We supplement the APOGEE DR17 abundance data with two different age catalogs. The first is from [Leung et al. \(2023\)](#), who train a variational encoder-decoder network on asteroseismic data for APOGEE red giants. This catalog has two main advantages over other neural network (NN) age estimates: their method is designed to reduce contamination from abundance information (in particular $[\alpha/\text{Fe}]$), and the recovered ages do not plateau at ~ 10 Gyr as they do in some other neural network-derived age catalogs (e.g., [Mackereth et al. 2019](#)). Following the recommendations of [Leung et al. \(2023\)](#), we cut all stars which have a relative age uncertainty greater

Table 1. Sample selection parameters from APOGEE DR17 (see Section 2).

Parameter	Range or Value	Notes
$\log g$	$1.0 < \log g < 3.8$	Select giants only
T_{eff}	$3500 < T_{\text{eff}} < 5500$ K	Reliable temperature range
S/N	$S/N > 80$	Required for accurate stellar parameters
ASPCAPFLAG Bits	$\notin 23$	Remove stars flagged as bad
EXTRATARG Bits	$\notin 0, 1, 2, 3, \text{ or } 4$	Select main red star sample only
NN age error	$\sigma_{\tau}/\tau < 40\%$	Age uncertainty from Leung et al. (2023)
R_{gal}	$3 < R_{\text{gal}} < 15$ kpc	Eliminate bulge & extreme outer-disk stars
$ z $	$ z < 2$ kpc	Eliminate halo stars

Table 2. Median and dispersion in APOGEE parameter uncertainties.

Parameter	Median Uncertainty	Uncertainty Dispersion (95% – 5%)
[Fe/H]	0.0089	0.0060
[O/Fe]	0.019	0.031
$\log_{10}(\tau_{\text{NN}}/\text{Gyr})$	0.10	0.16
$\tau_{[\text{C}/\text{N}]}/\text{Gyr}$	1.0	N/A

Table 3. Number of APOGEE stars in each Galactic region.

$R_{\text{gal}} \in$ $ z \in$	(3, 5] kpc	(5, 7] kpc	(7, 9] kpc	(9, 11] kpc	(11, 13] kpc	(13, 15] kpc
(1.0, 2.0] kpc	2013	2100	8734	3663	1324	363
(0.5, 1.0] kpc	2487	3490	13811	9069	3289	460
(0.0, 0.5] kpc	3296	7029	17319	16276	6336	812

than 40%. This produces a sample of 57 607 stars with NN age estimates, of which 14 871 are in the Solar neighborhood ($7 \leq R_{\text{gal}} < 9$ kpc, $0 \leq |z| < 0.5$ kpc). The median uncertainty in $\log(\text{age}/\text{Gyr})$ is 0.10 (see Table 2). We hereafter refer to the [Leung et al. \(2023\)](#) ages as “NN ages.”

Our second age catalog uses the [C/N]–age relation for red giant branch and red clump stars. **Paragraph describing [C/N]-derived ages (get help from Jack).** This method has the benefit of providing age estimates for luminous giants, which increases the sample size at larger distances from the Sun. However, systematic effects of the [C/N]–age relation mean that these ages are most trustworthy in the range $1 \sim 10$ Gyr. We estimate ages for 113 464 stars across the disk, including 20 995 in the Solar neighborhood. **Note about metallicity cutoff for luminous giants. Cite: Cao & Pinsonneault (2025)**

3. CHEMICAL EVOLUTION MODELS & PARAMETER SELECTION

We run multi-zone GCE models using the Versatile Integrator for Chemical Evolution (VICE; [Johnson & Weinberg 2020](#)). The basic format of our models follows [Johnson et al. \(2021\)](#) and [Dubay et al. \(2024\)](#). We

set up a disk with radial extent $0 \leq R_{\text{gal}} < 20$ kpc that is divided into concentric rings of width $\delta R_{\text{gal}} = 100$ pc. We use a time-step size of $\Delta t = 10$ Myr and a resolution of $n = 8$ stellar populations per time-step per ring, and we run our models up to a final time of $t_{\text{final}} = 13.2$ Gyr.

Within each ring, chemical evolution proceeds according to a conventional one-zone GCE model with instantaneous mixing and continuous recycling. Stellar populations migrate between zones as described in Section 3.6, allowing the long-lived progenitors of SNe Ia to enrich areas of the Galaxy outside of their birth zones. We inhibit star formation past $R_{\text{gal}} > 15.5$ kpc, so stars in the outer 4.5 kpc of the model disk represent a purely migrated population. We also assign a final midplane distance to each stellar population as described in Section 3.6. We do not incorporate radial gas flows between the different zones, but we discuss their potential implications in Section 5.3.

We discuss our assumptions about the nucleosynthetic yields in Section 3.1, the outflow prescription in Section 3.2, the gas supply in Section 3.3, the infall parameter selection in Section 3.4, the star formation law in Section 3.5, and the stellar migration prescription in Section 3.6.

Table 4 summarizes the most relevant variables and their fiducial values in this work.

3.1. Nucleosynthetic Yields

The population-averaged nucleosynthetic yields of CCSNe, y_{X}^{CC} , are uncertain to a degree that is significant for chemical evolution models. This problem is exacerbated by the complexity of the CCSN explosion landscape (Sukhbold et al. 2016). Recently, Weinberg et al. (2024) used a measurement of the mean Fe yield of CC SNe by Rodríguez et al. (2023) and the plateau in stellar $[\alpha/\text{Fe}]$ abundances at low metallicity to infer population-averaged yields of $y/Z_{\odot} \approx 1$ —in other words, for every $1 M_{\odot}$ of stars formed, massive stars release a mass of newly-synthesized α -elements (e.g., O or Mg) equal to their mass in the Sun. However, Johnson et al. (2024) found that GCE models with yields at this scale approach present-day abundances too slowly to match the observed age–metallicity relation. Previous multi-zone models using VICE (e.g., Johnson et al. 2021; Dubay et al. 2024) adopted higher yields ($y/Z_{\odot} \approx 2.6$) based on Chieffi & Limongi (2004) and Limongi & Chieffi (2006); however, in order to produce a realistic evolution of $[\text{O}/\text{Fe}]$, those studies adopted an integrated SN Ia rate which is high compared to the measurement of Maoz & Graur (2017).

We investigate yield sets at multiple scales of the Solar abundance. The CCSN yield of O is directly set by the Solar scale, $y_{\text{O}}^{\text{CC}} = (y/Z_{\odot})Z_{\text{O},\odot}$, because all O is assumed to form in CCSNe. For Fe, the CCSN yield is set by the $[\alpha/\text{Fe}]$ “plateau” at low metallicity, $[\alpha/\text{Fe}]_{\text{CC}}$, such that $y_{\text{Fe}}^{\text{CC}} = (y/Z_{\odot})Z_{\text{Fe},\odot}10^{-[\alpha/\text{Fe}]}$ (for further discussion on the empirical yield scale and the CCSN plateau, see Weinberg et al. 2024). We adopt the Asplund et al. (2009) Solar abundances: $Z_{\text{O},\odot} = 5.72 \times 10^{-3}$ and $Z_{\text{Fe},\odot} = 1.29 \times 10^{-3}$. Our yield sets are presented in Table 5. We consider $y/Z_{\odot} = 1$ representative of the empirical yield scale, whereas $y/Z_{\odot} = 2 - 3$ span a range of theoretical predictions.

The SN Ia yield of Fe, $y_{\text{Fe}}^{\text{Ia}}$, is set so that our models reach $[\text{O}/\text{Fe}] \approx 0.0$ by $t = 13.2$ Gyr. For $y/Z_{\odot} = 3$, the combined Fe yield of CCSNe and SNe Ia matches the Solar yield scale: $(y_{\text{Fe}}^{\text{Ia}} + y_{\text{Fe}}^{\text{CC}})/Z_{\text{Fe},\odot} = y/Z_{\odot}$; for $y/Z_{\odot} = 1$ and $y/Z_{\odot} = 2$, $y_{\text{Fe}}^{\text{Ia}}$ is increased from the given scale by a factor of 30% and 10%, respectively (rephrase). The fifth row of Table 5 reports the integrated SN Ia rate

$$\frac{N_{\text{Ia}}}{M_{\star}} = \frac{y_{\text{Fe}}^{\text{Ia}}}{\bar{m}_{\text{Fe}}^{\text{Ia}}} \quad (1)$$

from each yield set, assuming a mean Fe yield per SN Ia of $\bar{m}_{\text{Fe}}^{\text{Ia}} = 0.7 M_{\odot}$ (Mazzali et al. 2007; Howell et al. 2009). The rate for the $y/Z_{\odot} = 1$ yield set is

slightly higher than the volumetric rate of $N_{\text{Ia}}/M_{\star} = (1.3 \pm 0.1) \times 10^{-3} M_{\odot}^{-1}$ reported by Maoz & Graur (2017), but is consistent with their measurement of $N_{\text{Ia}}/M_{\star} = (1.6 \pm 0.3) \times 10^{-3} M_{\odot}^{-1}$ for field galaxies. The rate for the $y/Z_{\odot} = 2$ yield set is consistent with the measurement of $N_{\text{Ia}}/M_{\star} = (2.2 \pm 1.0) \times 10^{-3} M_{\odot}^{-1}$ by Maoz & Mannucci (2012), while the rate for the $y/Z_{\odot} = 3$ yield set is generally higher than literature values.

Unlike CCSNe, SNe Ia populate a broad distribution of delay times between progenitor formation and explosion. The time-dependent SN Ia rate in units of $M_{\odot}^{-1} \text{yr}^{-1}$ is defined as

$$R_{\text{Ia}}(t) = \begin{cases} \frac{N_{\text{Ia}}}{M_{\star}} \frac{f_{\text{Ia}}(t)}{\int_{t_D}^{t_{\text{max}}} f_{\text{Ia}}(t') dt'}, & t \geq t_D \\ 0 & t < t_D, \end{cases} \quad (2)$$

where $t_D = 40$ Myr is the minimum SN Ia delay time, $t_{\text{max}} = 13.2$ Gyr is the lifetime of the disk, N_{Ia}/M_{\star} is the total number of SNe Ia per unit mass of star formation, and $f_{\text{Ia}}(t)$ is the un-normalized form of the DTD. Motivated by the finding by Dubay et al. (2024) that a large fraction of long-delayed SNe Ia improves agreement with the Milky Way’s high- α sequence, we adopt a wide plateau DTD of the form

$$f_{\text{Ia}}(t) = \begin{cases} 1, & t < 1 \text{ Gyr} \\ (t/1 \text{ Gyr})^{-1.1}, & t \geq 1 \text{ Gyr}. \end{cases} \quad (3)$$

We discuss the implications of using a different DTD in Section 4.3.

Many previous two-infall studies have adopted the yields of François et al. (2004), who in turn adapted those of Woosley & Weaver (1995) for CCSNe and Iwamoto et al. (1999) for SNe Ia to provide a better fit between GCE models and local abundance data. Notably, the yields for O and Fe were left unchanged from the original studies. However, because Woosley & Weaver (1995) report gross yields without detailed initial abundances for their CCSN progenitors, and because François et al. (2004) do not provide population-averaged yields, it is difficult to make a comparison with our yield sets. Ultimately, François et al. (2004) report that their GCE models are insensitive to changes in the CCSN yield of O by a factor of 2, so we consider it reasonable to explore the full range of yields given in Table 5.

Figure 1 illustrates the effect of the yield scaling on the abundance evolution in one-zone models. We vary the outflow mass-loading factor η for each model to achieve a consistent endpoint to the abundance evolution (see Section 3.2 for further discussion on outflows). All models feature a rapid dilution of the ISM metallicity by

Table 4. A summary of variables and their fiducial values for our chemical evolution models (see discussion in Section 3).

Quantity	Fiducial Value	Alternatives	Section	Description
y/Z_\odot	1	2, 3	3.1	Scale of nucleosynthetic yields (see Table 5)
$f_{\text{Ia}}(t)$	Equation 3	Equation 15	3.1	Delay-time distribution of Type Ia supernovae
η_\odot	0.2	1.4, 2.4	3.2	Outflow mass-loading factor at R_\odot (see Table 5)
R_η	5.0 kpc	—	3.2	Exponential outflow scale radius
$f_\Sigma(R_\odot)$	0.12	0.25, 0.5	3.3	Local thick/thin disk surface density ratio
$[X/H]_{\text{CGM}}$	Pristine	-0.7, -0.5	3.3	Metallicity of infalling gas
τ_1	1 Gyr	0.1 – 3 Gyr	3.4	Timescale of the first infall epoch
$\tau_2(R_\odot)$	15 Gyr	3 – 30 Gyr	3.4	Timescale of the second infall epoch at the Solar annulus
R_{τ_2}	7 kpc	—	3.4	Exponential scale radius of the second infall timescale
t_{max}	4.2 Gyr	1 – 5 Gyr	3.4	Time of maximum gas infall (onset of second infall)
σ_{RM8}	2.68 kpc	3.6, 5.0 kpc	3.6	Radial migration strength

Table 5. Nucleosynthetic yields and outflow prescriptions.

	$y/Z_\odot = 1$ (empirical)	$y/Z_\odot = 2$ (theoretical)	$y/Z_\odot = 3$ (extreme)
y_{O}^{CC}	5.72×10^{-3}	1.14×10^{-2}	1.72×10^{-2}
$y_{\text{Fe}}^{\text{CC}}$	4.58×10^{-4}	9.15×10^{-4}	1.37×10^{-3}
y_{O}^{Ia}	0	0	0
$y_{\text{Fe}}^{\text{Ia}}$	1.08×10^{-3}	1.83×10^{-3}	2.50×10^{-3}
$N_{\text{Ia}}/M_\star [\text{M}_\odot^{-1}]$	1.55×10^{-3}	2.62×10^{-3}	3.57×10^{-3}
η_\odot	0.2	1.4	2.4

408 $\sim 0.5 - 0.8$ dex, visible in the top two panels, brought
 409 on by the infall of pristine gas at t_{max} . For the model
 410 with $y/Z_\odot = 1$, this dilution persists for some time and
 411 the metallicity does not return to Solar until the close to
 412 present day. The models with higher yields and outflows
 413 recover from this dilution more quickly, returning to So-
 414 lar metallicity by ~ 5 Gyr ago. However, the high-yield
 415 models experience a decline in $[\text{O}/\text{Fe}]$ of ~ 0.2 dex be-
 416 tween the second infall and the present day, contrasted
 417 with the smaller decline of ~ 0.1 dex in the low-yield
 418 model.

419 Figure 1 also indicates the mode of the APOGEE
 420 abundance distributions in 1 Gyr-wide age bins. As ex-
 421 plained by Johnson et al. (2024), the mode is expected
 422 to be less sensitive to the effects of radial migration than
 423 other statistical measures. The data show that the evo-
 424 lution in $[\text{O}/\text{H}]$ is close to flat over the past 5 Gyr. The
 425 behavior of the $y/Z_\odot = 2$ and $y/Z_\odot = 3$ models closely
 426 matches this trend in the data, whereas the $y/Z_\odot = 1$
 427 model increases significantly by ~ 0.2 dex during the
 428 same time period. The $[\text{Fe}/\text{H}]$ abundance in the data
 429 does increase slightly at late times, likely due to the de-

430 layed contribution of Fe from SNe Ia. Between lookback
 431 times of $\sim 5 - 9$ Gyr, the modes of $[\text{O}/\text{H}]$ and $[\text{Fe}/\text{H}]$ are
 432 higher than the present-day, likely due to a larger popu-
 433 lation of migrated stars relative to stars born in-situ at
 434 those times.

435 The three models in Figure 1 predict nearly iden-
 436 tical evolution in $[\text{O}/\text{Fe}]$ over the past 5 Gyr, and
 437 the trend in the data is similar apart from a ~ 0.05
 438 dex offset (which could be corrected by increasing $y_{\text{Fe}}^{\text{Ia}}$
 439 or adjusting the zero-point in the stellar abundances).
 440 The offset between the data and models grows between
 441 $\sim 5 - 8$ Gyr, especially for the higher yields. Of the
 442 three, the $y/Z_\odot = 2$ and $y/Z_\odot = 3$ models most closely
 443 match the observed late-time age-metallicity relations,
 444 whereas the $y/Z_\odot = 1$ model shows the best agreement
 445 with the observed $[\text{O}/\text{Fe}]$ evolution. As the $y/Z_\odot = 2$
 446 and $y/Z_\odot = 3$ models behave qualitatively similarly, we
 447 focus on the $y/Z_\odot = 1$ and $y/Z_\odot = 2$ yield sets for the
 448 remainder of this study.

3.2. Outflows

450 Mass-loaded outflows are a useful tool for scaling the
 451 endpoint of GCE models. Weinberg et al. (2017) showed
 452 that in the case of exponentially declining star forma-
 453 tion, the O abundance approaches an equilibrium at

$$Z_{\text{O,eq}} = \frac{y_{\text{O}}^{\text{CC}}}{1 + \eta - r - \tau_\star/\tau_{\text{SFH}}}, \quad (4)$$

455 where $r = 0.4$ is the instantaneous recycling parameter,
 456 τ_\star is the star formation efficiency timescale, τ_{SFH} is the
 457 star formation timescale, and $\eta \equiv \dot{\Sigma}_{\text{out}}/\dot{\Sigma}_\star$ is the out-
 458 flow mass-loading factor. Motivated by Equation 4, we
 459 adopt an outflow mass-loading factor at the Solar ra-
 460 dius $\eta_\odot \equiv \eta(R = R_\odot)$ for each of the yield sets in Table

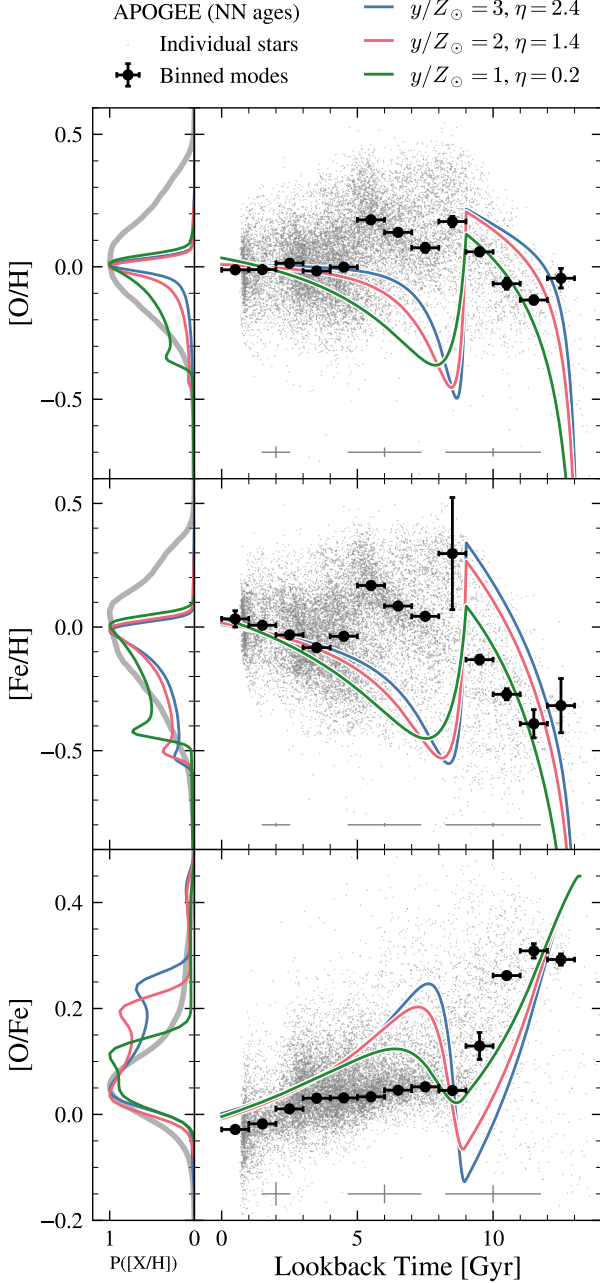


Figure 1. The abundance evolution of three one-zone models with different yield sets and outflow mass-loading factors. Table 5 presents the population-averaged yields for each model. The gray points plot the abundances of APOGEE stars with NN ages from Leung et al. (2023) from the Solar neighborhood ($7 \leq R_{\text{gal}} < 9 \text{ kpc}$, $0 \leq |z| < 0.5 \text{ kpc}$). The black points with error bars indicate the mode of the abundance data in 1 Gyr-wide age bins, and the gray error bars along the bottom of each panel indicate the median age and abundance errors as a function of age.

5. Models with lower yields do not achieve a steady-state abundance in time (see Figure 1); therefore, the values of η_{\odot} for $y/Z_{\odot} = 1$ and $y/Z_{\odot} = 2$ are lower than would be suggested by Equation 4 in order to reach Solar metallicity at the end of the model.

Equation 4 suggests that one can achieve a different $Z_{\text{O,eq}}$ in different regions of the Galaxy by adopting a spatially-varying prescription for η . In order to produce an exponentially declining radial metallicity gradient, we adopt a prescription for the outflow mass-loading factor which increases exponentially with radius:

$$\eta(R_{\text{gal}}) = \eta_{\odot} \exp\left(\frac{R_{\text{gal}} - R_{\odot}}{R_{\eta}}\right) \quad (5)$$

where R_{η} is the exponential outflow scale radius and $R_{\odot} = 8 \text{ kpc}$. As discussed by Johnson et al. (2024), an exponential trend in η with R_{gal} produces a linear trend in $[\text{O}/\text{H}]$ with R_{gal} . We adopt $R_{\eta} = 5 \text{ kpc}$, a lower value than in Johnson et al. (2024), so that our $y/Z_{\odot} = 1$ model produces a radial abundance gradient of $\nabla[\text{O}/\text{H}]_{\text{eq}} \approx -0.06 \text{ dex kpc}^{-1}$ (citations).

Most previous studies of the two-infall model have assumed that the Milky Way has experienced no significant mass-loaded outflows. Even in studies which do incorporate Galactic winds, the mass-loading is relatively weak (e.g., $\eta \approx 0.2$ in Palicio et al. 2023). To achieve a realistic radial metallicity gradient, many studies adopt the yields of François et al. (2004) and use a prescription for the infall timescale of the thin disk which increases linearly with radius (e.g., Chiappini et al. 1997; Romano et al. 2000). Additionally, many two-infall models reach a final metallicity higher than Solar. Citations for present-day gas abundance in the Solar neighborhood.

As discussed by Johnson et al. (2024), evidence for or against outflows in Milky Way-type galaxies in simulations and observations is inconclusive. Because we aim to study the effect of the yield assumptions on two-infall model predictions, we use mass-loaded outflows to control the final state of chemical evolution across the disk. However, mass-loaded outflows are not a necessary ingredient for the results of this study. We find that a one-zone model with the fiducial parameters, $\eta = 0$, and $y/Z_{\odot} = 0.8$, predicts a similar abundance evolution and nearly identical stellar abundance distributions to the model with $\eta = 0.2$ and $y/Z_{\odot} = 1$. Therefore, our multizone models with $y/Z_{\odot} = 1$ should predict similar behavior to a model without any mass-loaded outflows.

3.3. The Gas Supply

We run VICE in “infall mode,” where we specify the gas infall density $\dot{\Sigma}_{\text{in}}$ and the star formation efficiency (SFE) timescale $\tau_{\star} \equiv \Sigma_g / \dot{\Sigma}_{\star}$ as functions of time. The

gas surface density Σ_g and star formation rate $\dot{\Sigma}_\star$ are calculated from the two specified quantities according to our star formation law, which is described in Section 3.5, assuming zero initial gas mass in all zones.

The infall rate as a function of time and galactocentric radius can generically be described by

$$\dot{\Sigma}_{\text{in}}(t, R_{\text{gal}}) = A f_{\text{in}}(t | R_{\text{gal}}) g(R_{\text{gal}}), \quad (6)$$

where $g(R_{\text{gal}}) = \Sigma_\star(R_{\text{gal}})/\Sigma_\star(R_{\text{gal}} = 0)$ is the stellar density gradient, f_{in} is the infall rate over time, and A is the normalization. Because we incorporate mass-loaded outflows, A is not analytically solvable, so first we numerically integrate the star formation rate $\dot{\Sigma}_\star(t, R_{\text{gal}})$ and then follow the procedure outlined in Appendix B of Johnson et al. (2021) to calculate A . The infall rate is normalized to produce a total disk stellar mass of $(5.17 \pm 1.11) \times 10^{10} M_\odot$ (Licquia & Newman 2015) and to match the stellar surface density gradient of Bland-Hawthorn & Gerhard (2016).

The infall rate is described by two successive, exponentially declining bursts in time. The first infall component induces the formation of the thick disk, and the second component produces the thin disk. At a given galactocentric radius R_{gal} , the un-normalized form of the infall rate is

$$f_{\text{in}}(t | R_{\text{gal}}) = e^{-t/\tau_1} + f_{2/1}(R_{\text{gal}}) e^{-(t-t_{\text{max}})/\tau_2}, \quad (7)$$

where τ_1 and τ_2 are the first and second infall timescales, respectively, t_{max} is the onset of the second infall and thus the time of maximum gas infall, and $f_{2/1}$ is the ratio of the second infall amplitude to the first. We numerically calculate $f_{2/1}$ for each zone such that the resulting stellar density profile follows a two-component disk, with the surface density ratio of the thick and thin disks given by

$$f_\Sigma(R) \equiv \frac{\Sigma_1(R)}{\Sigma_2(R)} = f_\Sigma(R_\odot) e^{(R-R_\odot) \cdot (1/R_2 - 1/R_1)}. \quad (8)$$

We adopt a thick disk scale radius of $R_1 = 2.0 \text{ kpc}$, a thin disk scale radius of $R_2 = 2.5 \text{ kpc}$, and a fiducial value for the local surface density ratio of $f_\Sigma(R_\odot) = 0.12$ (Bland-Hawthorn & Gerhard 2016).

The thick-to-thin disk density ratio is especially important for our GCE models as it controls the quantity of gas accreted during each infall epoch. Our fiducial value of $f_\Sigma(R_\odot) = 0.12$ is on the low end of literature estimates, which range from $f_\Sigma(R_\odot) \sim 0.06 - 0.6$ (e.g., Gilmore & Reid 1983; Siegel et al. 2002; Jurić et al. 2008; Mackereth et al. 2017; Fuhrmann et al. 2017). Previous two-infall studies have adopted a similarly broad range of values (e.g., $f_\Sigma(R_\odot) = 0.18$ from Spitoni et al. 2021;

$f_\Sigma(R_\odot) = 0.4$ from Spitoni et al. 2024). We therefore explore values up to $f_\Sigma(R_\odot) = 0.5$ in our multi-zone models in Section 4.

In most of our models, we assume the infalling gas is pristine (i.e., $Z_{\text{in}} = 0$). However, the circumgalactic medium (CGM) from which the infalling gas is drawn could be previously enriched, either from gas stripped from dwarf galaxies or from SNe in the halo (citations; any measurements of CGM metallicity?). For this reason, we also test cases where the infalling gas is pre-enriched and its metallicity is described by

$$Z_{\text{in}}(t) = (1 - e^{-t/\tau_{\text{rise}}}) Z_\odot 10^{[\text{X}/\text{H}]_{\text{CGM}}}. \quad (9)$$

In this case, the metallicity rises from 0 with a timescale $\tau_{\text{rise}} = 2 \text{ Gyr}$ and plateaus at $[\text{X}/\text{H}]_{\text{CGM}} = [\text{O}/\text{H}]_{\text{CGM}} = [\text{Fe}/\text{H}]_{\text{CGM}}$. Previous GCE studies suggest that some level of enrichment of the infalling gas can improve agreement with observations (e.g., Palla et al. 2020; Johnson et al. 2024; Spitoni et al. 2024).

3.4. Infall Rate Parameter Selection

Previous studies have adopted a wide range of parameters for Equation 7. Figure 2 illustrates the effect of varying the infall parameters on gas abundance tracks and stellar abundance distributions in a one-zone model. The first infall timescale τ_1 , shown in panel (a), primarily affects the stellar distribution along the high- α sequence. Though τ_1 has an apparently large effect on the size of the low- α loop, the effect on the stellar abundance distribution of the low- α sequence is quite small due to the low number of stars formed between $t \sim 3 - 6 \text{ Gyr}$. We adopt $\tau_1 = 1 \text{ Gyr}$ for our fiducial value, in line with Spitoni et al. (2020) but longer than, e.g., Nissen et al. (2020) or Spitoni et al. (2021), in order to set the peak of the high- α sequence at $[\text{O}/\text{Fe}] \approx +0.3$.

Panel (b) of Figure 2 shows that the second infall timescale τ_2 controls the size of the low- α loop, which affects the width of the MDF and the low- α $[\text{O}/\text{Fe}]$ distribution. A shorter τ_2 produces a bigger loop and therefore a broader $[\text{O}/\text{Fe}]$ distribution which is skewed to higher $[\text{O}/\text{Fe}]$, while a longer τ_2 produces a smaller loop, leading to both a narrower low- α sequence and a narrower MDF. We note that our maximum value of $\tau_2 = 30 \text{ Gyr}$ is close to a constant infall rate, so a further increase in τ_2 has diminishing returns. Between $\tau_2 = 3 - 30 \text{ Gyr}$, the endpoint of the abundance tracks shifts by $\sim 0.2 \text{ dex}$ in $[\text{Fe}/\text{H}]$ and $\sim 0.1 \text{ dex}$ in $[\text{O}/\text{Fe}]$, which could affect the model's ability to reproduce the present-day abundance of the Solar neighborhood. We adopt a fiducial value of $\tau_2 = 15 \text{ Gyr}$ for the Solar neighborhood in order to minimize the size of the loop and width of the low- α $[\text{O}/\text{Fe}]$ distribution while still ap-

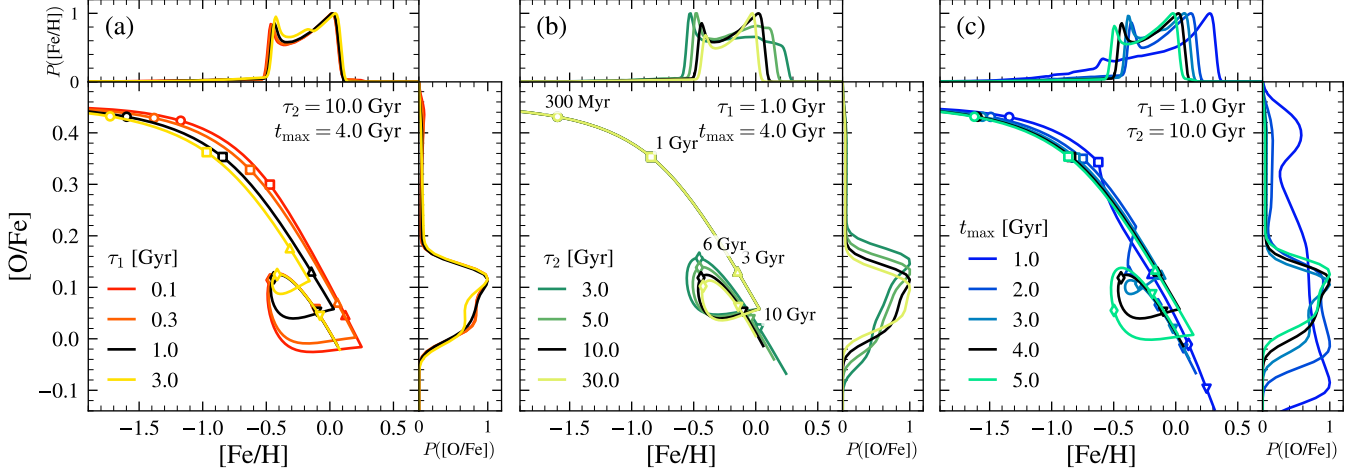


Figure 2. Gas abundance tracks in the $[O/Fe]$ – $[Fe/H]$ plane for one-zone chemical evolution models which assume different values for the infall history parameters. In each panel, one parameter is varied according to the legend while the other two are held fixed. The open symbols along each curve mark logarithmic steps in time, as denoted in panel (b). The marginal panels show the corresponding stellar abundance distributions, which are convolved with a Gaussian kernel with a width of 0.02 dex for visual clarity. All models use the $y/Z_{\odot} = 1$ yield set and assume $\eta = 0.2$.

proaching Solar $[Fe/H]$ at late times (see further discussion in Section 4.3). This value is in line with the infall timescale recovered by Spitoni et al. (2020), and similar to the local star formation timescale adopted by Johnson et al. (2021), but significantly longer than the timescales found by Nissen et al. (2020) and Spitoni et al. (2021).

In our multi-zone models, we vary the second infall timescale with radius to produce inside-out growth of the disk. Previous multi-zone two-infall studies (e.g., Chiappini et al. 2001; Palla et al. 2020) scale τ_2 linearly with radius, with $\tau_2 \approx 1$ Gyr in the inner disk and $\tau_2 = 7$ Gyr at the Solar annulus. This prescription was adopted to match the metallicity distribution of the Solar neighborhood and the bulge in the absence of mass-loaded outflows (Romano et al. 2000). We instead adopt an exponential $\tau_2 - R_{\text{gal}}$ relation, with $\tau_2(R_{\odot}) = 15$ Gyr at the Solar annulus and a scale radius $R_{\tau_2} = 7$ kpc. This is similar to the star formation history timescale of Johnson et al. (2021), which was based on the stellar age gradients in Milky Way-like spirals observed by Sánchez (2020). We also run models with a linear prescription and with a uniform value for τ_2 and find little difference in our key results.

Finally, panel (c) of Figure 2 shows that the time of maximum infall t_{max} (c) strongly affects the overall stellar abundance distribution for values $t_{\text{max}} \leq 2$ Gyr, but in this case the gas tracks do not produce the characteristic abundance loop. For $t_{\text{max}} > 2$ Gyr, varying t_{max} results in a minor shift to the mean of the MDF and little change to the $[O/Fe]$ distributions, even though the abundance tracks in $[O/Fe]$ – $[Fe/H]$ space appear very

different. The value of t_{max} also slightly adjusts the ISM abundance endpoint, as a longer t_{max} means the chemical evolution “reset” from the second infall occurs closer to the present day (see discussion in Section 4.1. We adopt a fiducial value of $t_{\text{max}} = 4.2$ Gyr, i.e. a look-back time of 9 Gyr, which is generally in line with previous two-infall studies (e.g., Nissen et al. 2020; Spitoni et al. 2020, 2021). This ensures that our models are compatible with the median age of the thick disk in the APOKASC-3 catalog of 9.14 ± 0.05 Gyr (Pinsonneault et al. 2025).

The Milky Way’s last major merger with the dwarf galaxy dubbed Gaia Sausage-Enceladus (GSE; Belokurov et al. 2018; Helmi et al. 2018) has been proposed as an important influence on the transition from the thick disk to the thin disk, as in Spitoni et al. (2024). Our fiducial value of $t_{\text{max}} = 4.2$ Gyr places the start of the formation of the thin disk close to the GSE merger (within uncertainties), which likely occurred ~ 10 Gyr ago (e.g., Helmi et al. 2018; Gallart et al. 2019; Naidu et al. 2021; Woody et al. 2025).

We note that all our models are normalized to produce the same thick-to-thin-disk mass ratio of $f_{\Sigma}(R_{\odot}) = 0.12$ (Bland-Hawthorn & Gerhard 2016) at the Solar annulus regardless of the infall parameters. The high- α sequence appears much less prominent in our $[O/Fe]$ distributions in Figure 2 than in the data because the model outputs include only stars which were formed in-situ at the Solar annulus. In our multi-zone models, most of the high- α stars present in the Solar neighborhood have migrated from the inner Galaxy.

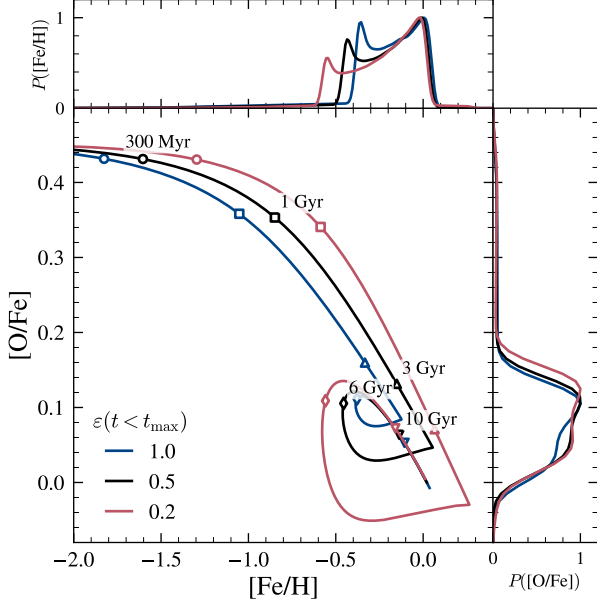


Figure 3. Effect of the SFE timescale pre-factor ε on abundance tracks and distributions in a one-zone model (see Section 3.5). All models are normalized to produce roughly the same ratio of thick to thin disk stars regardless of the value of ε during the first infall epoch.

3.5. The Star Formation Law

The star formation law follows a single power-law prescription: $\dot{\Sigma}_\star \propto \Sigma_g^N$, with $N = 1.5$ following Kennicutt (1998). Previous work with this GCE model (e.g., Johnson et al. 2021; Dubay et al. 2024) assumed a three-component power-law, but we adopt a single power-law prescription in this work to allow for a more direct comparison with previous two-infall studies (e.g., Spitoni et al. 2024).

In detail, we calculate the star formation efficiency (SFE) timescale $\tau_\star \equiv \Sigma_g / \dot{\Sigma}_\star$ according to the following:

$$\tau_\star = \begin{cases} \varepsilon(t)\tau_{\text{mol}}(t), & \Sigma_g \geq \Sigma_{g,0} \\ \varepsilon(t)\tau_{\text{mol}}(t) \left(\frac{\Sigma_g}{\Sigma_{g,0}} \right)^{-1/2}, & \Sigma_g < \Sigma_{g,0} \end{cases} \quad (10)$$

where $\Sigma_{g,0} = 10^8 \text{ M}_\odot \text{ kpc}^{-2}$ and $\tau_{\text{mol}}(t) = \tau_{\text{mol},0}(t/t_0)^\gamma$, with $\gamma = 1/2$, $t_0 = 13.8 \text{ Gyr}$ (?) and $\tau_{\text{mol},0} = 2 \text{ Gyr}$ Leroy et al. (2008). Previous two-infall studies (e.g., Nissen et al. 2020) have adopted a higher SFE during the first infall epoch than during the second, which we emulate through the pre-factor ε :

$$\varepsilon(t) = \begin{cases} 0.5, & t < t_{\text{max}} \\ 1.0, & t \geq t_{\text{max}}. \end{cases} \quad (11)$$

A lower value of $\varepsilon(t < t_{\text{max}})$ leads to more efficient star formation during the first infall epoch. Figure 3 illus-

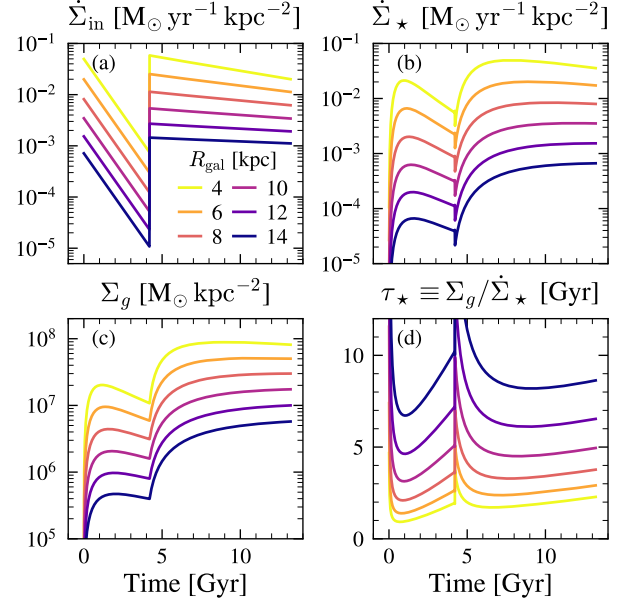


Figure 4. (a) The infall surface density, (b) the star formation surface density, (c) the gas surface density, and (d) the star formation efficiency timescale as a function of time for our fiducial multi-zone model with $y/Z_\odot = 1$. Each panel plots the history for six different zones of width $\delta R_{\text{gal}} = 0.1 \text{ kpc}$, color-coded by Galactocentric radius.

trates that this pre-factor largely affects the metallicity of the high- α sequence, with a smaller ε producing faster enrichment during the first infall and stronger dilution after t_{max} . The pre-factor has virtually no effect on the overall $[\text{O}/\text{Fe}]$ distribution because the model is normalized to produce the same thick-to-thin-disk mass ratio regardless of the details of the star formation law, but a lower value of ε does narrow the MDF by ~ 0.1 dex in $[\text{Fe}/\text{H}]$. We adopt $\varepsilon(t < t_{\text{max}}) = 0.5$ for consistency with the two-infall literature. To guard against over-correcting the SFE in the early Galaxy, we have tested eliminating either $\varepsilon(t)$ or $\tau_{\text{mol}}(t)$ from our SFE prescription in multi-zone models and found no substantial difference to our results.

Figure 4 plots the star formation history of several different zones from our fiducial model with $y/Z_\odot = 1$. In the inner Galaxy, the infall rate $\dot{\Sigma}_{\text{in}}$ is similar at the start of the first and second infall epochs, and the star formation rate peaks at $t \approx 7 \text{ Gyr}$. In the outer Galaxy, the infall rate at t_{max} is significantly higher than at $t = 0$, and the star formation rate is highest at the present day. The star formation efficiency timescale τ_\star spikes near $t = 0$ and t_{max} , but otherwise increases throughout the model's duration, reaching a maximum of $\tau_\star \approx 2 \text{ Gyr}$ in the inner disk and $\tau_\star \approx 9 \text{ Gyr}$ in the outer disk.

3.6. Stellar Migration

This study is not the first to apply a prescription for radial migration to a two-infall GCE model. [Spitoni et al. \(2015\)](#) explored the effect of migration speeds of order $\sim 1 \text{ km s}^{-1}$ on the metallicity distribution of the Solar neighborhood. They prescribed some fraction of stars from the inner and outer Galaxy which contribute to the local present-day population based on a constant migration speed, and they also assumed some fraction of stars born in the Solar neighborhood will have migrated elsewhere. This method can improve agreement with the observed local metallicity distribution, but does not scale to abundance distributions across the disk. [Palla et al. \(2022\)](#) compared the [Spitoni et al. \(2015\)](#) prescription to the diffusion treatment of [Frankel et al. \(2018\)](#) and found similar results. Our implementation, described below, affects abundance distributions across the Galaxy, not just at the Solar annulus.

The distance a stellar population born at R_{form} migrates over its age τ is drawn from a Gaussian centered at 0 with standard deviation

$$\sigma_{\text{RM}} = \sigma_{\text{RM8}} \left(\frac{\tau}{8 \text{ Gyr}} \right)^{0.33} \left(\frac{R_{\text{form}}}{8 \text{ kpc}} \right)^{0.61}, \quad (12)$$

where we adopt $\sigma_{\text{RM8}} = 2.68 \text{ kpc}$ as the fiducial value for the strength of radial migration. This is smaller than the value of $\sigma_{\text{RM8}} = 3.6 \text{ kpc}$ found by [Frankel et al. \(2018\)](#), but in Section 4.1 we explore the effect of a stronger migration prescription.

All stellar populations are born at the Galactic midplane and are assigned a final midplane distance z drawn from the distribution

$$p(z|\tau, R_{\text{final}}) = \frac{1}{4h_z} \text{sech}^2\left(\frac{z}{2h_z}\right), \quad (13)$$

where R_{final} is the final Galactocentric radius of the stellar population. The width of the distribution h_z is given by

$$h_z(\tau, R_{\text{final}}) = \left(\frac{0.24 \text{ kpc}}{e^2} \right) \exp\left(\frac{\tau}{7 \text{ Gyr}} + \frac{R_{\text{final}}}{6 \text{ kpc}} \right). \quad (14)$$

We note that the final midplane distance is assigned at the end of the model run and therefore does not affect the chemical evolution.

The parameters of Equations 12 and 14 were chosen to fit the stellar migration patterns in the **h277** hydrodynamical simulation ([Christensen et al. 2012](#)). A more complete discussion of the migration scheme and its consequences can be found in Appendix C of [Dubay et al. \(2024\)](#).

We note an important distinction between our method and that of [Spitoni et al. \(2015\)](#): SNe Ia from long-lived progenitors contribute Fe to each zone they migrate

through, not just their birth zone. This is important because the median delay time of our SN Ia DTD is $\sim 2 \text{ Gyr}$, for which the width of the migration distribution is $\sigma_{\text{RM}} \approx 2 \text{ kpc}$ (Equation 12). So, a significant fraction of SN Ia progenitors born in a given zone will enrich a disparate region of the Galaxy.

4. MULTI-ZONE MODEL RESULTS

4.1. Dilution & Approach to Equilibrium

The dilution effect discussed in Section 3.1 is clearly seen in the multi-zone model results. We first examine the differences between multi-zone models which assume different yield and outflow scales. Figure 5 shows stellar age–abundance relations produced by models with $y/Z_{\odot} = 1$ and $y/Z_{\odot} = 2$ with fiducial parameters (Table 4). The $y/Z_{\odot} = 1$ model (column a) shows two clear discrepancies with the [Leung et al. \(2023\)](#) age–abundance relation: a major $\sim 0.5 \text{ dex}$ dilution at a lookback time of $\sim 9 \text{ Gyr}$ near where the data show a maximum in $[\text{O}/\text{H}]$, and non-zero abundance evolution at late times where the data show very little abundance evolution. The evolution of $[\text{Fe}/\text{H}]$ is similar, but the approach to the final metallicity is slower because of the additional delay imposed on Fe production from SNe Ia. The $y/Z_{\odot} = 2$ yield set (column b) mitigates both of these issues by shortening the time it takes the ISM metallicity to rebound post- t_{max} , producing a much flatter abundance curve at late times. However, model (b) produces a poorer fit to the age- $[\text{O}/\text{Fe}]$ relation: the decline in $[\text{O}/\text{Fe}]$ over the thin disk epoch is steeper than the data, especially for ages $\sim 4 - 8 \text{ Gyr}$.

We next attempt to mitigate the dilution and late-time evolution problems for the empirical ($y/Z_{\odot} = 1$) yield scale. Figure 6 shows the effect of varying several parameters for the $y/Z_{\odot} = 1$ model: (b) the strength of radial migration σ_{RM8} , (c) the metallicity of the infalling gas $[\text{X}/\text{H}]_{\text{CGM}}$, and (d) the local thick-to-thin disk density ratio $f_{\Sigma}(R_{\odot})$.

The observed rise in the median metallicity of stars with ages of $\sim 4 - 10 \text{ Gyr}$ could be due to radial migration, as those stars were probably not born in-situ, but rather migrated from the dense inner metal-rich regions of the Galaxy ([Feuillet et al. 2018](#)). Although our fiducial model does include a prescription for radial migration, the majority of stars in that age range in Figure 5 still have sub-Solar abundances. Therefore, column (b) of Figure 6 presents a model with $y/Z_{\odot} = 1$ and a stronger migration prescription of $\sigma_{\text{RM8}} = 5 \text{ kpc}$. As a result, the stars which make up the present-day Solar neighborhood are drawn from a wider range of birth R_{gal} , producing a broader abundance distribution for any given age. However, even though this prescrip-

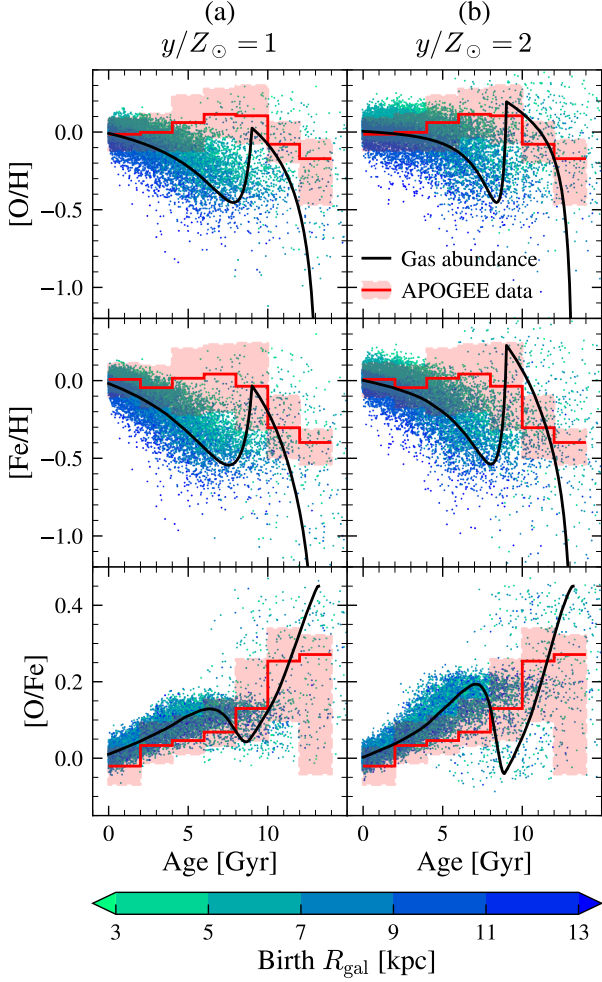


Figure 5. Stellar age–abundance relations produced by multi-zone models which assume different yield sets and out-flow mass-loading factors. Each point represents a stellar population drawn from the Solar neighborhood near the mid-plane ($7 \leq R_{\text{gal}} \leq 9 \text{ kpc}$, $0 \leq |z| \leq 0.5 \text{ kpc}$) and is color-coded by its birth radius. A Gaussian scatter is applied to each point according to the median age and abundance uncertainties in Table 2. For visual clarity, we plot only a random mass-weighted sample of 10 000 points in each panel. The black curve plots the ISM abundance at $R_{\text{gal}} = 8 \text{ kpc}$ over time. The red line segments plot the median abundance for APOGEE stars in 2 Gyr-wide age bins, and the shaded regions represent the 16th–84th percentiles in each bin. Age estimates for APOGEE stars come from Leung et al. (2023). **Key takeaway:** Both models feature a major dilution event at a lookback time of 9 Gyr, and for model (a) the dilution persists throughout much of the thin disk epoch.

tion is much stronger than the estimates of, e.g., Frankel et al. (2018), the model still significantly under-predicts the metallicity of $\sim 4 - 9 \text{ Gyr}$ old stars.

Next, we investigate a model where the infalling gas is enriched to a metallicity $[\text{O}/\text{H}] = [\text{Fe}/\text{H}] = [\text{X}/\text{H}]_{\text{CGM}}$

before accreting onto the disk. Column (c) of Figure 6 shows results for the case where $[\text{X}/\text{H}]_{\text{CGM}} = -0.5$, the highest metallicity allowed by the local low- α population (reword). Pre-enriched infall at this level mitigates but does not completely solve the two discrepancies. The dilution effect of the second infall is reduced to the ~ 0.3 -dex level as the gas which replenishes the Galaxy’s reservoir is no longer pristine; however, the width of the stellar abundance distribution at any given age is also reduced, because the enriched gas accretion imposes a lower limit on the metallicity of the outermost regions, from which the stars of the low-metallicity tail in the Solar neighborhood are drawn. The late-time gas abundance evolution is similar to the fiducial model, but it ends at slightly super-Solar metallicity—an effect which can be compensated by a slightly increased value of η . This model also narrows the $[\text{O}/\text{Fe}]$ distribution of mono-age populations (almost all the model stars fall within the 1σ band of the data), which could be compensated for by stronger radial migration.

Finally, we explore a model where the local thick-to-thin disk surface density ratio is ~ 4 times larger than the fiducial value, $f_{\Sigma}(R_{\odot}) = 0.5$. This is higher than most of the constraints from population counts or GCE models (see Section 3.3). Column (d) of Figure 6 shows that requiring a more massive thick disk can reduce the dilution and recent evolution of the ISM, similar to the pre-enriched infall, because more of the gas disk is built up during the first infall phase. The model produces the best agreement with the observed age– $[\text{Fe}/\text{H}]$ relation (second row). However, agreement with the observed age– $[\text{O}/\text{Fe}]$ relation is poor, with the model predicting less evolution in $[\text{O}/\text{Fe}]$ over the past $\sim 9 \text{ Gyr}$ than observed by $\approx 0.1 \text{ dex}$.

Overall, no modification to the $y/Z_{\odot} = 1$ model is able to completely overcome both the dilution and late-time evolution issues. Pre-enrichment of the accreted gas and a higher disk mass ratio can reduce the discrepancy with the data, but they cause issues of their own in the age– $[\text{O}/\text{Fe}]$ plane.

4.2. Abundance Evolution Across the Disk

The discrepancies between the predicted and observed abundance evolution discussed in Section 4.1 are also seen across the disk. Figure 7 shows the evolution of the MDF with age across five radial bins for the $y/Z_{\odot} = 1$ and $y/Z_{\odot} = 2$ models. We adopt pre-enriched infall ($[\text{Fe}/\text{H}]_{\text{CGM}} = -0.7$), stronger radial migration ($\sigma_{\text{RMS}} = 3.6 \text{ kpc}$), and a higher disk mass ratio ($f_{\Sigma}(R_{\odot}) = 0.25$) because these parameters were able to improve agreement with observations in previous sections. For the APOGEE sample, we use the $[\text{C}/\text{N}]$ -

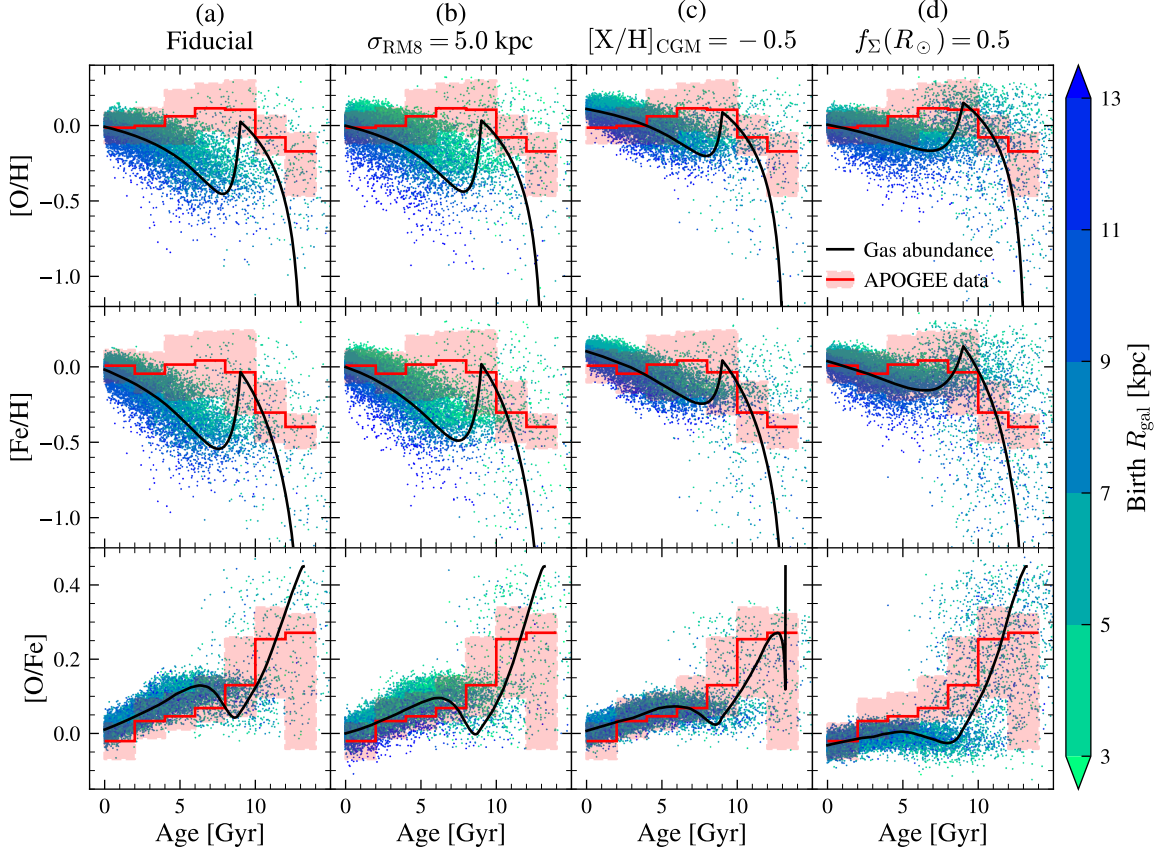


Figure 6. Stellar age–abundance relations in the Solar annulus produced by select multi-zone models with $y/Z_{\odot} = 1$. The layout is similar to Figure 5. Each column shows results from a different multi-zone model: **(a)** our fiducial model with $y/Z_{\odot} = 1$, $\sigma_{\text{RMS}} = 2.7$ kpc, pristine gas infall, and $f_{\Sigma}(R_{\odot}) = 0.12$; **(b)** a model with greater radial migration strength $\sigma_{\text{RMS}} = 5$ kpc; **(c)** a model that assumes the infalling gas has metallicity $[\text{O}/\text{H}]_{\text{CGM}} = [\text{Fe}/\text{H}]_{\text{CGM}} = -0.5$; and **(d)** a model with a higher local thick-to-thin disk ratio, $f_{\Sigma}(R_{\odot}) = 0.5$. **Key takeaway:** Model (d) comes the closest to the observed age–metallicity relation at the expense of the age– $[\text{O}/\text{Fe}]$ relation, but no model completely reconciles the dilution problem.

derived age estimates due to the larger sample size in the most distant regions of the disk; we limit the comparison to ages ≤ 10 Gyr because of large systematic uncertainties for the oldest stars, as discussed in Section 2.

The two-infall model predicts a very broad MDF for ages > 10 Gyr because of the rapid enrichment of the ISM during the first infall epoch.

Figure 7 shows that even with pre-enriched infall, both of our models predict that the MDF shifts to the left going from younger to older populations. On the other hand, the data show that the MDF broadens with age, which we attribute to radial migration, but its peak does not shift substantially over the past $\sim 6 - 8$ Gyr. While the mode of the MDF shifts depending on the radial bin, its evolution is remarkably consistent over the entire disk, in line with the equilibrium scenario of Johnson et al. (2024). *Note about metallicity cutoff for luminous giants.*

On the other hand, the model predictions for the MDF in the 8 – 10 Gyr age bin are strikingly similar to the APOGEE MDF. The two-infall model predicts a bimodal distribution: the metal-rich component comprises stars formed during the last Gyr of the first infall epoch, and the metal-poor component is stars formed during the first Gyr of the second infall epoch (post-dilution). The data show this same bimodal structure in all but the outermost radial bin, with peaks at $[\text{Fe}/\text{H}] \approx -0.3$ and $+0.3$. While the location of the model peaks depends on R_{gal} , in the data they are quite consistent from the innermost to the outermost bin. *I actually think the two-infall model gets this right for the wrong reasons. In the data, the left peak is the high- α sequence and the right is the high-metallicity end of the low- α sequence. In the model, the right peak is produced during the first infall (i.e., thick disk) and the left is immediately after the second infall (i.e., low-metallicity end of thin disk).*

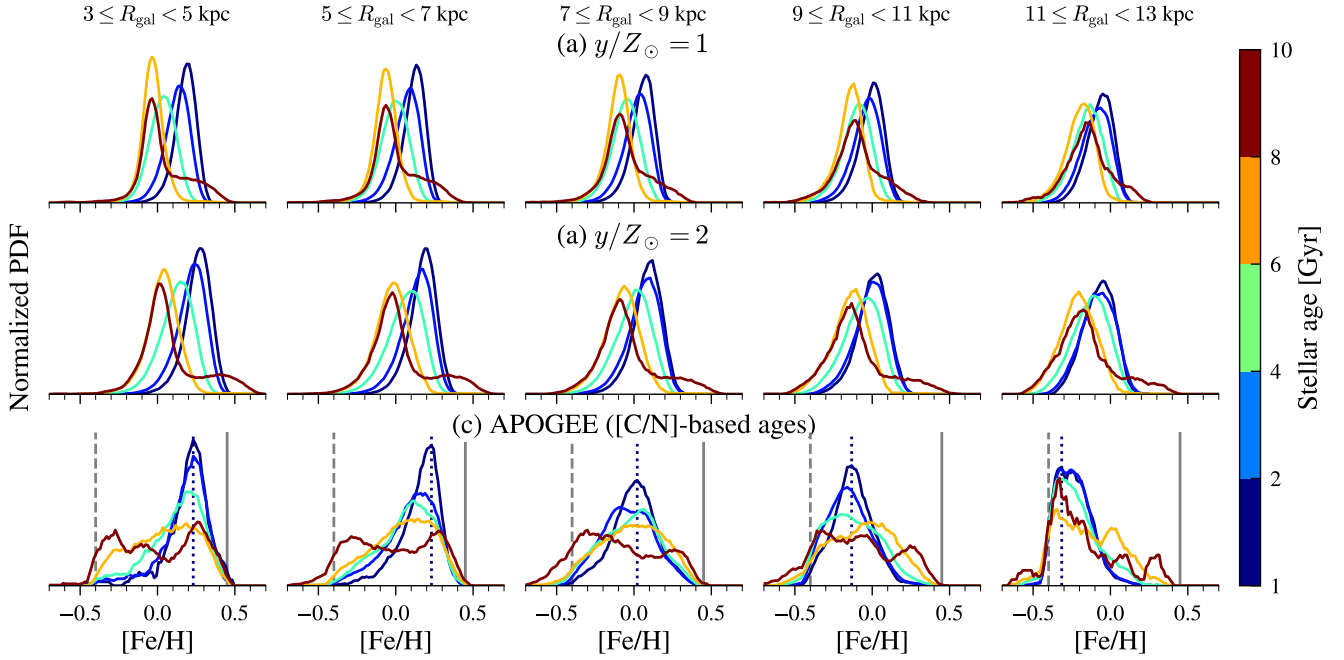


Figure 7. Evolution of the MDF across the Galactic disk. Each panel presents normalized stellar $[\text{Fe}/\text{H}]$ distributions as a function of stellar age within a 2 kpc-wide annulus. Rows (a) and (b) present the distributions from multi-zone GCE models with different yield scales. For both models we adopt the following non-fiducial parameters: $[\text{Fe}/\text{H}]_{\text{CGM}} = -0.7$, $\sigma_{\text{RMS}} = 3.6$ kpc, and $f_{\Sigma}(R_{\odot}) = 0.25$. A Gaussian scatter has been applied to each model stellar population in rows (a) and (b) according to the median age and abundance uncertainties in Table 2. Row (c) presents the distributions from APOGEE DR17 with ages derived from $[\text{C}/\text{N}]$ abundances (see Section 2). The vertical blue dotted lines in row (c) mark the mode of the distribution in the 1 – 2 kpc age bin for reference. Also in row (c), the gray dashed line marks the cut at $[\text{Fe}/\text{H}] > -0.4$ for upper red giant branch and red clump stars, and the gray solid line marks the cut at $[\text{Fe}/\text{H}] < +0.45$ for all stars with $[\text{C}/\text{N}]$ -based ages. Distributions in all panels are restricted to $0 \leq |z| < 0.5$ kpc and boxcar-smoothed with a width of 0.1 dex for visual clarity. **Key takeaway:** The APOGEE data show remarkably little variation in the mode at all radii over the past $\sim 6 - 8$ Gyr, while both GCE models produce a steady evolution toward higher $[\text{Fe}/\text{H}]$ with time.

4.3. The Local Abundance Topology

The two-infall model explains the chemical evolution of the thin disk through the low- α loop (see discussion in Section 3.4). However, inspection of the marginal $[\text{O}/\text{Fe}]$ distributions in, e.g., Figure 1 reveals a different morphology of the low- α sequence: the two-infall model predicts two peaks in $[\text{O}/\text{Fe}]$ in the thin disk where the data show only one. The location of the second peak, at intermediate $[\text{O}/\text{Fe}]$, varies depending on the yields (Figure 1) and infall parameters (Figure 2), but is always present. This morphology remains essentially consistent in our multi-zone models as well, despite the inclusion of radial mixing and vertical dispersion of stars.

Figure 8 illustrates the origin of the intermediate- α peak predicted by the two-infall model at mid to high Galactic latitudes. Between $0.5 \leq |z| < 1$ kpc, both the models with $y/Z_{\odot} = 1$ and $y/Z_{\odot} = 2$ predict an over-density of stars near the abundance turn-over ($[\text{Fe}/\text{H}] \approx -0.3$, $[\text{O}/\text{Fe}] \approx 0.1 - 0.2$), which is not seen in the APOGEE sample. This over-density occurs be-

cause the overall rate of chemical evolution slows down ~ 2 Gyr after the second infall, and at the same time the delayed enrichment from SNe Ia reverses the evolution of $[\text{O}/\text{Fe}]$. This is a generic prediction of *any* two-infall model regardless of its specific parameters, though its impact can be mitigated through parameter choices which act to compress the distance between the low- and intermediate- α peaks, as in the $y/Z_{\odot} = 1$ model in Figure 1 or the models with longer τ_2 in Figure 2.

Additionally, the shape of the low- α sequence in the model results (a concave-down “comma”) is clearly different from the data (a concave-up “swoosh”). **Not sure what this means because the inside-out SFH has the same issue. Maybe it’s related to radial migration?**

4.4. Global Abundance Distributions

4.4.1. The $[\text{O}/\text{Fe}]$ Distribution: Two or Three Peaks?

The two-infall model generically predicts *three* peaks in the $[\text{O}/\text{Fe}]$ distribution, which correspond to the high- α sequence, the abundance “turn-over” after the second

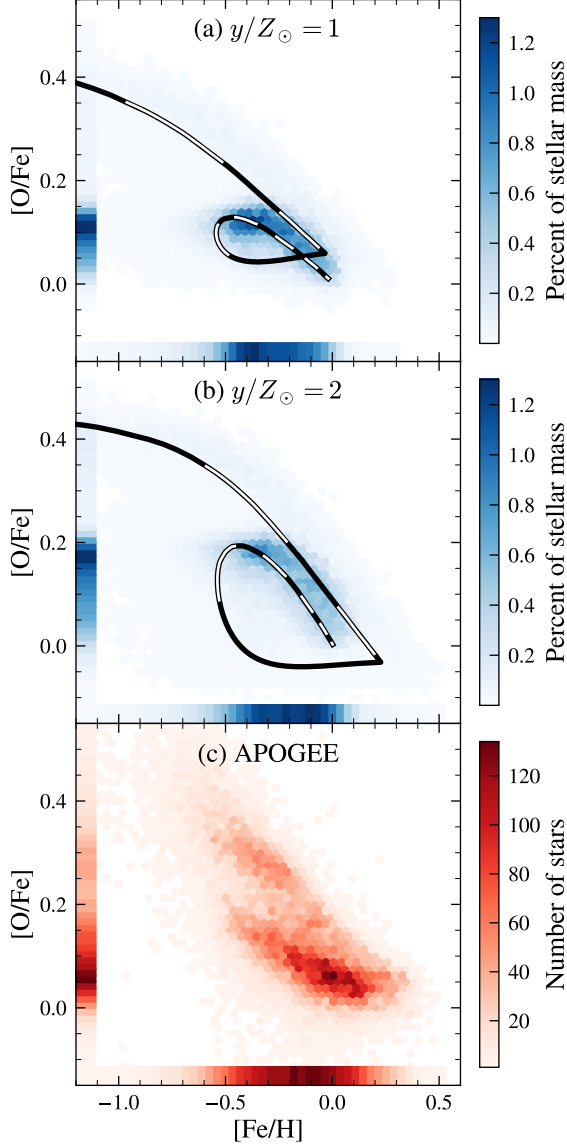


Figure 8. The density of stars in the $[\text{O}/\text{Fe}]$ – $[\text{Fe}/\text{H}]$ plane from multi-zone models with (a) $y/Z_{\odot} = 1$ and (b) $y/Z_{\odot} = 2$, and (c) from the APOGEE DR17 catalog. The curves in panels (a) and (b) plot the ISM abundance of the Solar annulus over time, and the alternating black and white segments mark time intervals of 1 Gyr. Stars are restricted to the region defined by $7 \leq R_{\text{gal}} < 9 \text{ kpc}$ and $0.5 \leq |z| < 1 \text{ kpc}$ to highlight the α -bimodality in the Solar neighborhood. **Key takeaway:** the two-infall model generically predicts a stellar overdensity at intermediate $[\text{O}/\text{Fe}]$ and low metallicity, which is not observed in APOGEE.

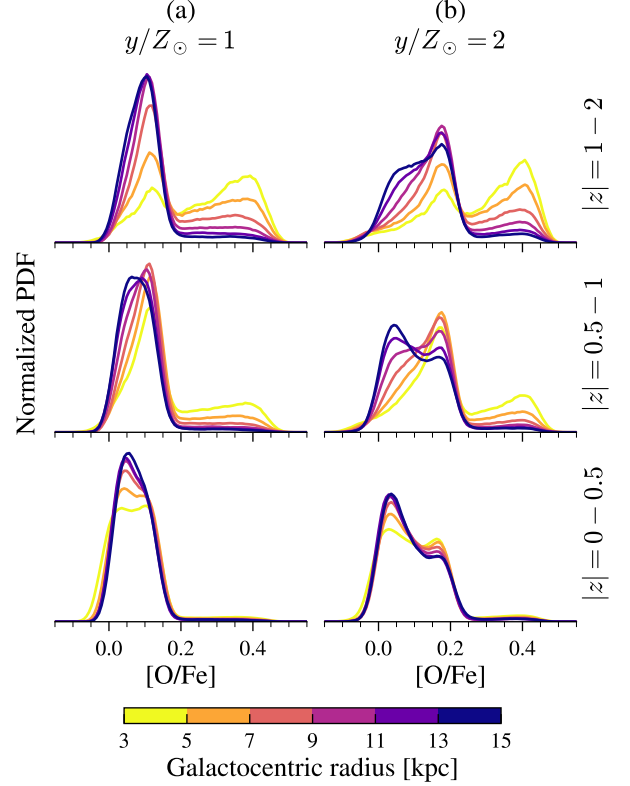


Figure 9. Normalized stellar $[\text{O}/\text{Fe}]$ distributions produced by multi-zone models which assume different yield sets and outflow mass-loading factors. Each row presents stellar distributions within a range of absolute midplane distance $|z|$ reported on the far right, and the vertical scale is consistent across each row. Within each panel, the distributions are color-coded according to the bin in galactocentric radius R_{gal} from which they are drawn. The median APOGEE abundance uncertainties are forward-modeled onto the model outputs (see Table 2). For visual clarity, each distribution is smoothed with a box-car of width 0.05 dex. **Key takeaway:** The two-infall model produces an intermediate- $[\text{O}/\text{Fe}]$ peak that is especially prominent in the $y/Z_{\odot} = 2$ model at mid to high latitudes.

infall, and finally the late-time low- α sequence. We previously noted this feature in Dubay et al. (2024). Figure 9 compares $[\text{O}/\text{Fe}]$ distributions from across the Galactic disk produced by models with the $y/Z_{\odot} = 1$ and $y/Z_{\odot} = 2$ yield sets. For model (a) with $y/Z_{\odot} = 1$, the

two thin disk peaks are close enough together that they approximate a single peak, especially once observational uncertainties are factored in. With the $y/Z_{\odot} = 2$ yield set, however, there is a ~ 0.2 dex separation between the low- and intermediate- α peaks thanks to increased efficiency of CCSN element production. As a result, model (b) predicts a high density of stars at $[\text{O}/\text{Fe}] \approx +0.2$ where the data show a relatively low density.

Discuss why we divided Figures 9 and 10 into $|z|$ bins: (1) pattern changes as a function of midplane distance, and (2) we don't have to worry so much about correcting the APOGEE data to rebalance between the thin and thick disk fields.

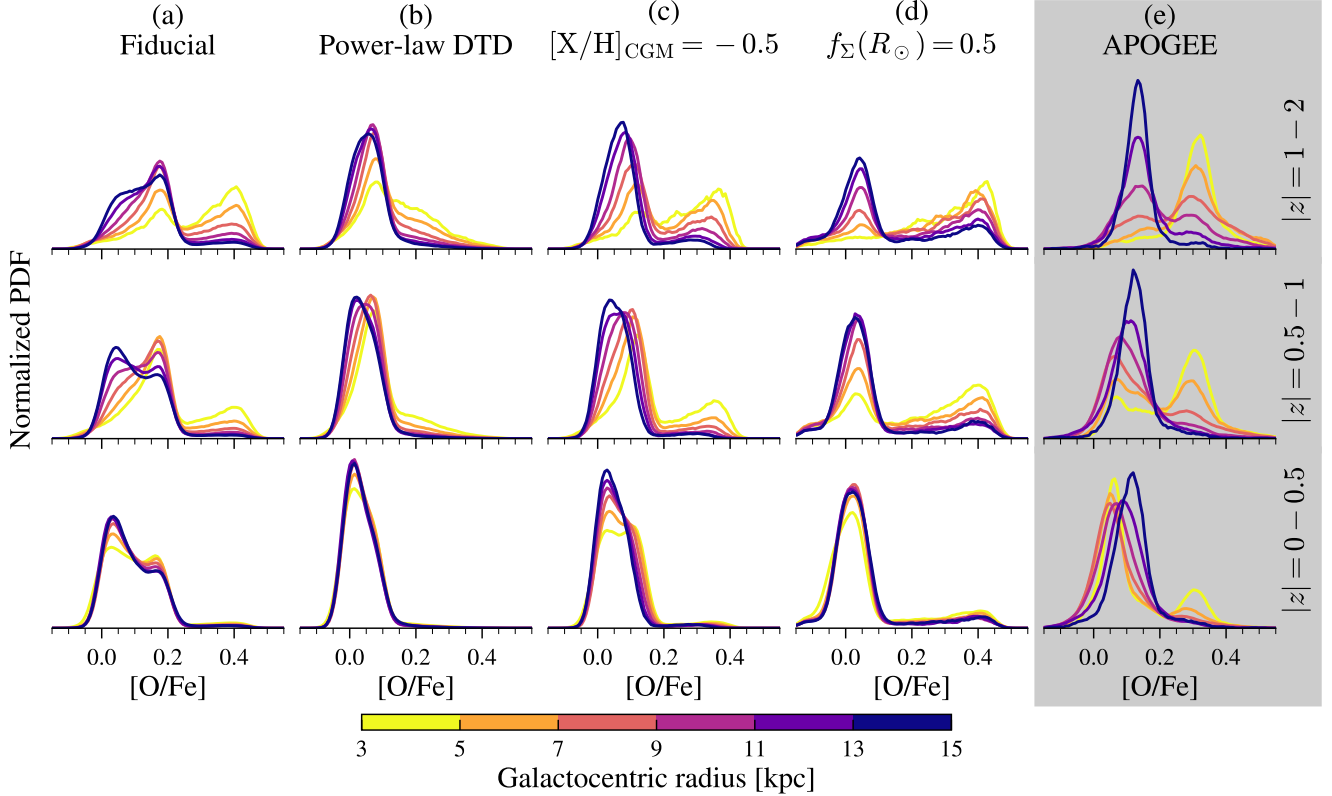


Figure 10. Stellar $[\text{O}/\text{Fe}]$ distributions produced by select multi-zone models with $y/Z_{\odot} = 2$ (a–d) and as observed by APOGEE (e). The layout is similar to Figure 9. Each column shows results from a different multi-zone model: **(a)** the fiducial model with $y/Z_{\odot} = 2$, the fiducial DTD, pristine gas infall, and $f_{\Sigma}(R_{\odot}) = 0.12$ (identical to column (b) of Figure 5); **(b)** a model that adopts a power-law DTD; **(c)** a model that assumes the infalling gas has metallicity $[\text{O}/\text{H}]_{\text{CGM}} = [\text{Fe}/\text{H}]_{\text{CGM}} = -0.5$; and **(d)** a model with a higher local thick-to-thin disk ratio, $f_{\Sigma}(R_{\odot}) = 0.5$. **Key takeaway:** For the $y/Z_{\odot} = 2$ case, pre-enrichment of the accreted gas or a higher thick-to-thin disk ratio can improve the low- α distribution while preserving the high- α peak.

In Figure 10, we show the result of our attempts to mitigate the intermediate- α peak discrepancy for the $y/Z_{\odot} = 2$ yield set in a few different ways, namely by reducing the size of the thin disk loop seen in panel (b) of Figure 8. First, we substitute our fiducial SN Ia DTD with a simple power-law,

$$f_{\text{Ia}}^{\text{plaw}}(t) = (t/1 \text{ Gyr})^{-1.1}, \quad (15)$$

which reduces the median SN Ia delay time from ~ 2 Gyr to ~ 0.5 Gyr. As shown in column (b), this has the intended effect on the low- α sequence, but it also entirely eliminates the high- α peak. Dubay et al. (2024) discuss in detail why such a DTD is disfavored by Milky Way stellar abundances, and their results hold true for the two-infall model as well.

Next, in model (c) the metallicity of the infalling gas increases to $[\text{X}/\text{H}]_{\text{CGM}} = -0.5$ at late times. We choose this value because if it were any higher, the infalling gas would have higher metallicity than the most metal-poor thin disk stars. This model results in very similar $[\text{O}/\text{Fe}]$ distributions to the $y/Z_{\odot} = 1$ case. We assume that the

infalling gas has $[\text{O}/\text{Fe}] = 0$ at all times; an alternate run with $[\text{O}/\text{Fe}] = +0.3$ shifted the distribution towards higher $[\text{O}/\text{Fe}]$, worsening agreement with observations.

Finally, in model (d) we increase the local thick-to-thin disk surface density ratio by a factor of 4 to $f_{\Sigma}(R_{\odot}) = 0.5$. This value means that 1 in 3 stars in the Solar annulus belong to the thick disk and is on the high end of estimates (citations). The result as shown in Figure 10 is a true bimodal abundance distribution, with a more prominent high- α peak than in the previous models. **Note that APOGEE high- α sequence is over-emphasized by survey selection function.** In summary, either pre-enriched infall or an enhanced disk mass ratio can improve agreement with the observed thin disk abundances for the $y/Z_{\odot} = 2$ case. These parameters also help the model better fit the age-metallicity relation, as shown in Section 4.1 for the $y/Z_{\odot} = 1$ case.

4.4.2. The Best Model

Motivated by the results of the previous sections, we construct a model which attempts to solve all of the

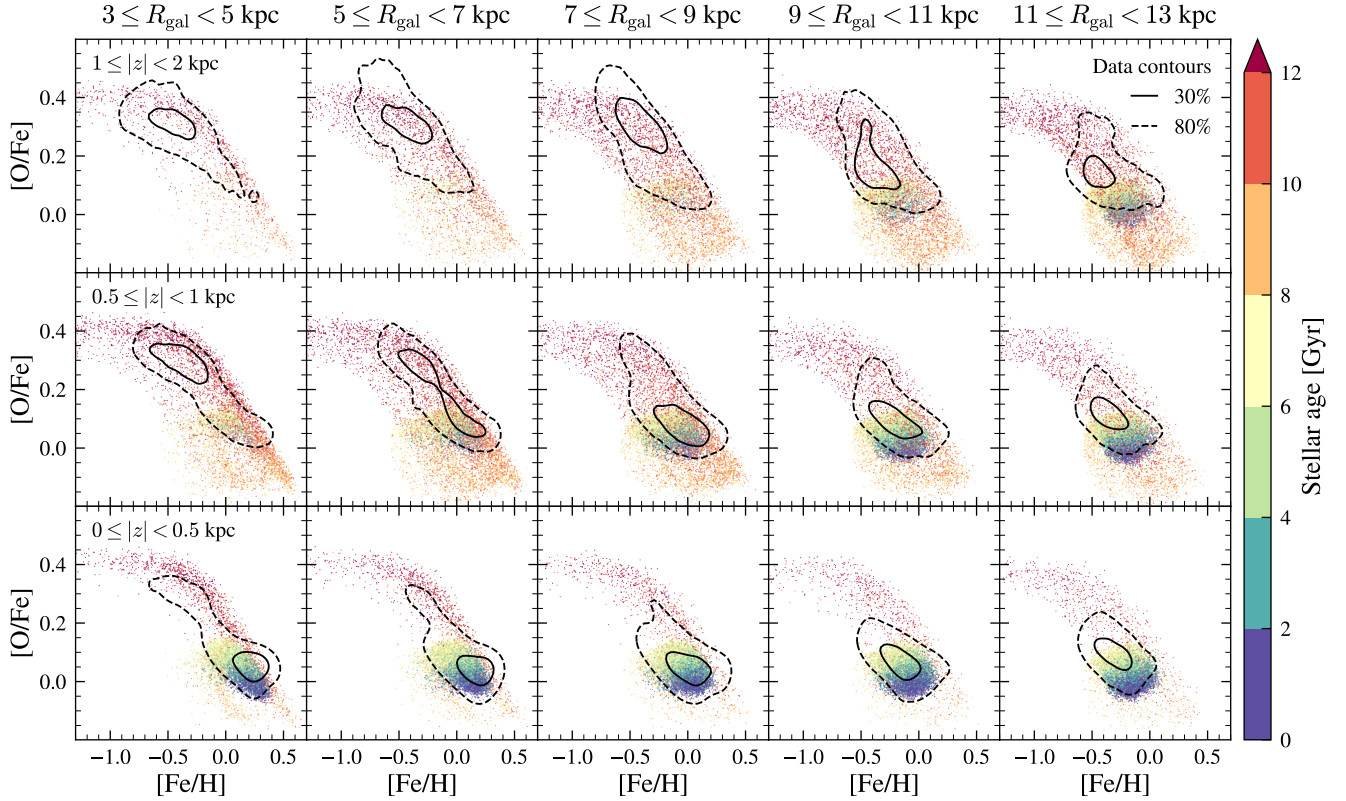


Figure 11. Stellar abundance distributions across the disk predicted by our best multi-zone model, with $y/Z_{\odot} = 2$, $[X/H]_{\text{CGM}} = -0.7$, $f_{\Sigma}(R_{\odot}) = 0.25$, $\sigma_{\text{RM8}} = 3.6 \text{ kpc}$, and $\eta_{\odot} = 1.8$. Each panel presents a random mass-weighted sample of 10 000 stellar populations that are drawn from the given $(R_{\text{gal}}, |z|)$ bin and color-coded by age. A Gaussian scatter is applied to each point according to the median age ($\tau_{[\text{C/N}]}$) and abundance uncertainties in Table 2. The solid and dashed contours enclose 30% and 80%, respectively, of the APOGEE data in each region. **Key takeaway:** The predicted distribution from the two-infall model lines up with the APOGEE distribution close to the midplane, but agreement is worse at higher latitudes and in the outer Galaxy.

issues that have been outlined thus far. Our “best attempt” model uses the $y/Z_{\odot} = 2$ yield set to flatten the local age–metallicity relation (Figure 5), pre-enriched infall at the level of $[X/H]_{\text{CGM}} = -0.7$ to reduce the dilution at t_{max} (Figure 6), slightly stronger outflows with $\eta_{\odot} = 1.8$ to maintain the local equilibrium at Solar metallicity, moderately stronger radial migration with $\sigma_{\text{RM8}} = 3.6 \text{ kpc}$ to widen the local metallicity dispersion (Figure 6), and a greater local disk ratio $f_{\Sigma}(R_{\odot}) = 0.25$ to reduce the width of the low- α distribution and beef up the high- α sequence (Figure 10). Our choices for $[X/H]_{\text{CGM}}$, σ_{RM8} , and $f_{\Sigma}(R_{\odot})$ are more moderate, and we believe more realistic, than in previous sections to avoid extreme effects resulting from the combination of these parameters. We stress that our focus is on qualitative rather than quantitative agreement with the data, and thus we do not attempt to find the optimal set of parameters through methods such as MCMC.

Figure 11 presents the stellar $[\text{O}/\text{Fe}]$ – $[\text{Fe}/\text{H}]$ –age distributions as a function of R_{gal} and $|z|$ predicted by the

best multi-zone model. The model is generally successful at reproducing the observed distribution of stars in the $[\text{O}/\text{Fe}]$ – $[\text{Fe}/\text{H}]$ plane, especially in the inner Galaxy and close to the midplane (panels along the left and bottom sides of the figure, respectively). However, the predicted high- α sequence is less concentrated than in the data, and its presence is still significant even in the outer Galaxy—likely a consequence of the stronger migration prescription and higher thick-to-thin disk ratio. In general, the predicted distributions do not align with the data quite as well at large midplane distances ($1 \leq |z| < 2 \text{ kpc}$), but this may partly be due to our prescription for vertical heating (see Section 3.6).

The model makes two notable predictions about the age–abundance distributions. First, there is a population of $\sim 8 - 9 \text{ Gyr}$ old stars at sub-Solar $[\text{O}/\text{Fe}]$, especially at $|z| \geq 0.5 \text{ kpc}$, formed immediately after the second infall during a period of rapid chemical evolution. These stars form a small percentage of the overall distribution (see also Figure 11 from Spitoni et al. 2024) but

in this case they occupy a unique portion of the abundance space. A longer τ_1 could shift this population to higher $[\text{O}/\text{Fe}]$ where it would be obscured by the rest of the low- α sequence (see Figure 2). Second, the stars born at the tail end of the thick and thin disk epochs are adjacent to each other in abundance space, meaning the two-infall model predicts a steep age gradient for the most metal-rich stars in a given region.

4.5. Local Age Patterns

The two-infall model makes a prediction about the local stellar age distribution that is fundamental to its construction: that the most metal-rich stars born in-situ in any region of the Galaxy come from the metal-rich tail of the first infall sequence, and are therefore older than all of the thin disk stars. As noted in the previous Section, this prediction is apparent in any of the panels in Figure 11, especially where $|z| < 0.5$ kpc. We investigate this prediction further here.

The top row of Figure 12 presents the median stellar age as a function of $[\text{O}/\text{Fe}]$ and $[\text{Fe}/\text{H}]$ for two multi-zone models and APOGEE. While the models predict a fairly accurate distribution of stars in abundance space, especially for the low- α population, the stellar age patterns are obviously quite different. In both the $y/Z_\odot = 1$ and $y/Z_\odot = 2$ models, there is a sharp divide in the median stellar age when moving from the thick disk ($\tau \geq 9$ Gyr) to the thin disk ($\tau \lesssim 5$ Gyr). The $y/Z_\odot = 2$ model also predicts that the stars with the lowest $[\text{O}/\text{Fe}]$ should be $\sim 8 - 9$ Gyr old, while these are some of the youngest stars in APOGEE. The latter issue can be mitigated by adjusting the parameters of the first infall, as discussed in the previous Section, but the former is not solved so easily.

We further highlight the discrepant age patterns in the bottom panels of Figure 12, which compare the overall stellar age distribution against that of the locally metal rich (LMR) stars, defined here as $[\text{Fe}/\text{H}] \geq +0.1$.¹ For APOGEE, the distributions are similar, both peaking near ~ 5 Gyr, although very few of the LMR stars have ages $\gtrsim 10$ Gyr. Our two-infall models produce an age distribution for the overall sample that is similar to the data, but for LMR stars, both models predict a distinctly bimodal age distribution. There is a large contribution from the young, metal-rich end of the second infall, and a contribution from the old, metal-rich end of the first, but there are few stars in between. The trough between the modes lies at ~ 5 Gyr for both models, right where the APOGEE distribution peaks.

¹ The precise location of the cut matters little, as we observe the same behavior for cuts ranging from +0.05 to +0.2 dex.

Mention some ways to try to resolve this (e.g., stronger radial migration) and that they don't work. Note that our projected log age error of 0.1 dex is accurate for stars < 8 Gyr old, but too large for older stars, so the scatter in the high- α sequence is larger than the data.

5. DISCUSSION

Summary of problem: the two-infall model is boxed in by data.

5.1. The Empirical Yield Scale

The $y/Z_\odot = 1$ empirical yield scale already has difficulties matching the local age-metallicity relation (Johnson et al. 2024), but the problem is exacerbated in the two-infall case because of the delayed dilution event — in effect, approach to equilibrium is “reset” by the second infall.

5.2. Third Accretion Episode

Talk about Spitoni et al. (2023); Palla et al. (2020). Some combination of metal-rich accretion and radial gas flows might reduce the amount of dilution predicted by a recent accretion episode.

5.3. Radial Gas Flows

Radial gas flows are hard :(Some two-infall studies (e.g., Spitoni & Matteucci 2011; Palla et al. 2020, 2024) implement inward radial gas flows with velocity ~ 1 km s⁻¹ in order to reproduce the radial abundance gradient without Galactic outflows.

Spitoni & Matteucci (2011) find that a two-infall model of the disk without gas exchange produces a radial metallicity gradient which is too shallow. They implement an inward radial gas flow on the order of $\sim 0 - 4$ km s⁻¹ which varies with radius, and find that it improves agreement with the observed gradient. However, they found that a variable star formation efficiency with radius in combination with a gas density threshold for star formation could also reproduce the observed gradient without radial flows.

5.4. Star Formation Hiatus

The two-infall model falls into the broader category of GCE models which reproduce the α -bimodality by halting or severely limiting star formation for some duration. For the two-infall model, this phase of low star formation immediately precedes the second infall epoch and is due to the relatively short timescale of the first infall epoch. However, as we have shown, the dilution of the ISM resulting from the second infall poses a challenge when comparing to age-abundance data.

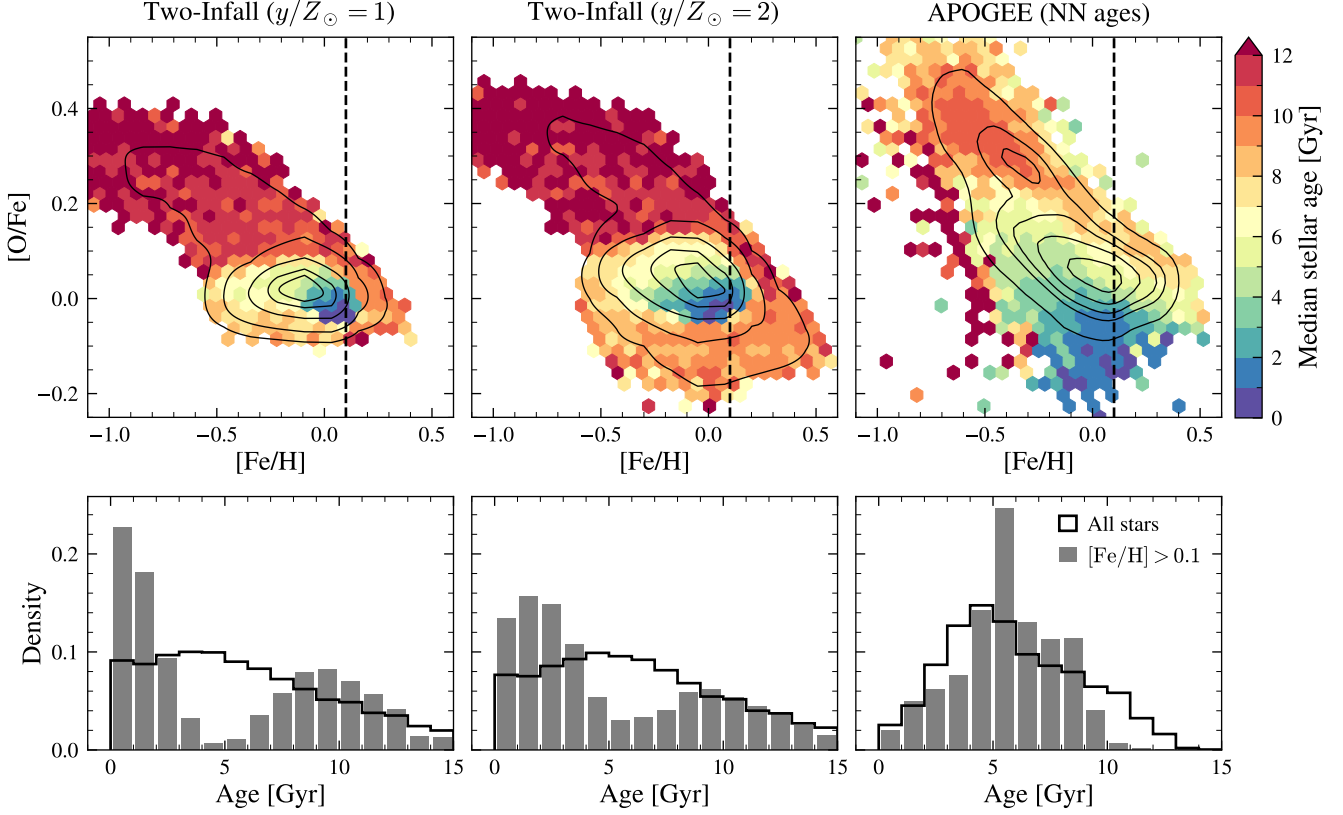


Figure 12. *Top:* The median stellar age as a function of [O/Fe] and [Fe/H] in the Solar annulus ($7 \leq R_{\text{gal}} < 9 \text{ kpc}$, $0 \leq |z| < 2 \text{ kpc}$). The left and center panels plot the output of our best two-infall models, with $y/Z_{\odot} = 2$, $[X/H]_{\text{CGM}} = -0.7$, $f_{\Sigma}(R_{\odot}) = 0.25$, and $\sigma_{\text{RM8}} = 3.6 \text{ kpc}$. The model output has been re-sampled to match the APOGEE stellar $|z|$ distribution, and a Gaussian scatter has been applied to the abundances and ages according to Table 2. The right panel plots the results from APOGEE using the Leung et al. (2023) age catalog. The contours indicate the density of stars in the [Fe/H]–[O/Fe] plane, and the vertical dashed line denotes the boundary for locally metal-rich (LMR) stars. *Bottom:* Stellar age distributions in the Solar annulus for all stars (black) and LMR stars (gray). The left and center panels plot the mass-weighted age distributions predicted by the models after forward-modeling age uncertainties, and the right panel plots the Leung et al. (2023) ages for APOGEE stars. **Key takeaway:** The two-infall model predicts a fundamentally different age pattern than what is observed, especially for LMR stars.

A bursty infall history is not the only way to produce a gap in the star formation history. Beane et al. (2024) present a simulated galaxy from the Illustris TNG50 suite that exhibits MW-like bimodality. They argue that the α -bimodality is brought on by a brief ($\sim 300 \text{ Myr}$) quiescent period caused by bar formation. The virial mass of their galaxy grows steadily throughout this period, unlike in our two-infall model where the mass grows by a factor of ~ 2 during the 1 Gyr following the second infall.

While our semi-analytic model does not include a Galactic bar, we can explore the effects of a star formation hiatus by artificially boosting the SFE timescale τ_{\star} for a period of time. Figure 13 illustrates the effect of this SFE-driven hiatus in a one-zone model with an exponentially declining infall rate. During the quiescent period, the [O/Fe] ratio slowly declines due to the de-

layed contribution of Fe from SNe Ia. Meanwhile, the gas mass continues to increase even as star formation is suppressed. When τ_{\star} is lowered at the end of the quiescent period, the high gas mass sparks a moderate star formation burst which causes stellar abundances to “pile up” at similar [O/Fe] values. The trough between the high- and low- α sequences results from the star formation returning to pre-quiescence behavior.

Our simple hiatus model offers a few parameters which control the chemical evolution. The onset time of the SFE hiatus controls the position of the high- α sequence: a later onset places the peak at lower [O/Fe]. The duration of the star formation hiatus (and the τ_{\star} enhancement factor?) controls the strength of the high- α peak.

The parameters of the SFE hiatus in Figure 13 were chosen to match the APOGEE stellar [O/Fe] distribution as closely as possible. However, there are some

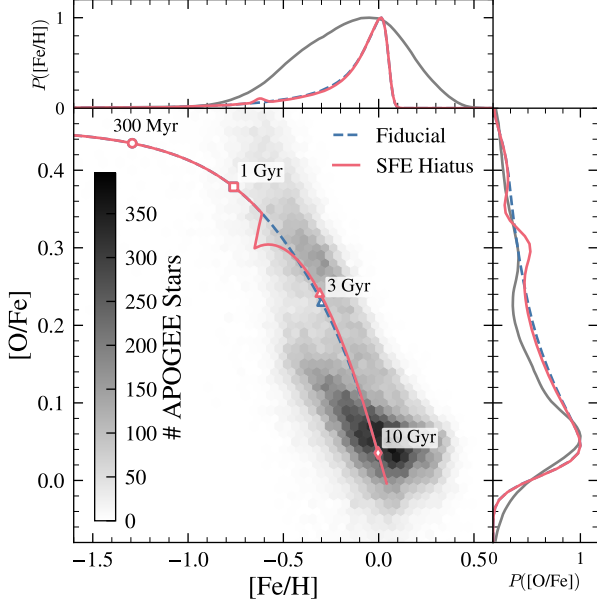


Figure 13. Abundance tracks and distributions from one-zone models which experience an efficiency-driven starburst. The blue dashed curve represents the fiducial model that has an exponentially declining infall rate and constant star formation efficiency timescale $\tau_\star = 2$ Gyr. The red solid curve plots the output of a model which experiences an enhancement of τ_\star by a factor of 10, for a duration of 200 Myr, starting at $t = 1.4$ Gyr. Both models assume the $y/Z_\odot = 2$ yield set, with $y_{\text{Fe}}^{\text{Ia}}$ reduced by 20% to better match the model endpoint with the data, and $\eta = 1.4$. The greyscale histogram presents the number density of APOGEE stars in the Solar annulus ($7 \leq R_{\text{gal}} \leq 9$ kpc, $0 \leq |z| \leq 2$ kpc) in $[\text{O}/\text{Fe}]-[\text{Fe}/\text{H}]$ space, and the gray histograms in the marginal panels show the APOGEE stellar abundance distributions.

differences in detail, such as the dearth of stars at $[\text{O}/\text{Fe}] \approx +0.35$ due to the star formation hiatus. We intend this model to illustrate another path to reproducing the α -bimodality. Most of the high- α stars present in the Solar annulus have likely migrated from the inner Galaxy, where perhaps this SFE-driven hiatus was concentrated.

6. CONCLUSIONS

- The large quantity of pristine gas accreted in the Solar neighborhood during the second infall phase rapidly dilutes the ISM metallicity by ~ 0.5 dex. Models with low nucleosynthetic yields ($y/Z_\odot = 1$) remain at sub-Solar metallicity until the present day, in stark contrast to the observed local age-metallicity relation. Models with higher yields and outflows approach the present-day metallicity more rapidly, while pre-enriched infall can reduce

the magnitude of the dilution (but not eliminate it entirely).

- The “turn-over” in the evolution of $[\text{O}/\text{Fe}]$ following the second infall produces a double-peaked low- α sequence with a fundamentally different abundance structure than observed, especially for models with higher yields. A low yield set ($y/Z_\odot = 1$) coupled with lower outflows, or pre-enrichment of the infalling gas, can bring the stellar $[\text{O}/\text{Fe}]$ distributions more in line with the data.
- For metal-rich stars, the two-infall model predicts a sharp divide in the stellar age distribution between the thick and thin disk populations. In contrast, the data show a smooth gradient between the oldest and youngest stars, with most of the metal-rich stars having intermediate ages.
- Our models predict that the MDF evolves to higher metallicity over time throughout the disk. This contrasts with the APOGEE data, which show very little change in the mode over the past $\sim 6 - 8$ Gyr.
- The equilibrium scenario of chemical evolution, if correct, places stricter limits on the two-infall model than other evolutionary models.

ACKNOWLEDGEMENTS

Personal acknowledgements.

LOD and JAJ acknowledge support from National Science Foundation grant no. AST-2307621. JAJ and JWJ acknowledge support from National Science Foundation grant no. AST-1909841. LOD acknowledges financial support from an Ohio State University Fellowship. JWJ acknowledges financial support from an Ohio State University Presidential Fellowship and a Carnegie Theoretical Astrophysics Center postdoctoral fellowship. **Update grants and fellowships.**

Funding for the Sloan Digital Sky Survey IV has been provided by the Alfred P. Sloan Foundation, the U.S. Department of Energy Office of Science, and the Participating Institutions.

SDSS-IV acknowledges support and resources from the Center for High Performance Computing at the University of Utah. The SDSS website is www.sdss4.org.

SDSS-IV is managed by the Astrophysical Research Consortium for the Participating Institutions of the SDSS Collaboration including the Brazilian Participation Group, the Carnegie Institution for Science, Carnegie Mellon University, Center for Astrophysics — Harvard & Smithsonian, the Chilean Participation Group, the French Participation Group, Instituto de

1238 Astrofísica de Canarias, The Johns Hopkins Univer-
 1239 sity, Kavli Institute for the Physics and Mathematics
 1240 of the Universe (IPMU) / University of Tokyo, the Ko-
 1241 rean Participation Group, Lawrence Berkeley National
 1242 Laboratory, Leibniz Institut für Astrophysik Potsdam
 1243 (AIP), Max-Planck-Institut für Astronomie (MPIA Hei-
 1244 delberg), Max-Planck-Institut für Astrophysik (MPA
 1245 Garching), Max-Planck-Institut für Extraterrestrische
 1246 Physik (MPE), National Astronomical Observatories of
 1247 China, New Mexico State University, New York Uni-
 1248 versity, University of Notre Dame, Observatório Na-
 1249 cional / MCTI, The Ohio State University, Pennsylva-
 1250 nia State University, Shanghai Astronomical Observa-
 1251 tory, United Kingdom Participation Group, Universidad
 1252 Nacional Autónoma de México, University of Arizona,
 1253 University of Colorado Boulder, University of Oxford,
 1254 University of Portsmouth, University of Utah, Univer-
 1255 sity of Virginia, University of Washington, University of
 1256 Wisconsin, Vanderbilt University, and Yale University.
 1257 This work has made use of data from the Euro-
 1258 pean Space Agency (ESA) mission *Gaia* ([https://www.](https://www.cosmos.esa.int/gaia)
 1259 [cosmos.esa.int/gaia](https://www.cosmos.esa.int/gaia)), processed by the *Gaia* Data Pro-

1260 cessing and Analysis Consortium (DPAC, [https://www.](https://www.cosmos.esa.int/web/gaia/dpac/consortium)
 1261 [cosmos.esa.int/web/gaia/dpac/consortium](https://www.cosmos.esa.int/web/gaia/dpac/consortium)). Funding
 1262 for the DPAC has been provided by national institu-
 1263 tions, in particular the institutions participating in the
 1264 *Gaia* Multilateral Agreement.

1265 We would like to acknowledge the land that The Ohio
 1266 State University occupies is the ancestral and contem-
 1267 porary territory of the Shawnee, Potawatomi, Delaware,
 1268 Miami, Peoria, Seneca, Wyandotte, Ojibwe and many
 1269 other Indigenous peoples. Specifically, the university re-
 1270 sides on land ceded in the 1795 Treaty of Greenville
 1271 and the forced removal of tribes through the Indian Re-
 1272 moval Act of 1830. As a land grant institution, we want
 1273 to honor the resiliency of these tribal nations and rec-
 1274 ognize the historical contexts that has and continues to
 1275 affect the Indigenous peoples of this land.

1276 *Software:* VICE (Johnson & Weinberg 2020), Astropy
 1277 (Astropy Collaboration et al. 2013, 2018, 2022), scikit-
 1278 learn (Pedregosa et al. 2011), SciPy (Virtanen et al.
 1279 2020), Matplotlib (Hunter 2007).

APPENDIX

A. REPRODUCIBILITY

1282 **Blah.**

REFERENCES

- 1283 Abdurro’uf, Accetta, K., Aerts, C., et al. 2022, The
 1284 Astrophysical Journal Supplement Series, 259, 35,
 1285 doi: [10.3847/1538-4365/ac4414](https://doi.org/10.3847/1538-4365/ac4414)
- 1286 Asplund, M., Grevesse, N., Sauval, A. J., & Scott, P. 2009,
 1287 Annual Review of Astronomy and Astrophysics, 47, 481,
 1288 doi: [10.1146/annurev.astro.46.060407.145222](https://doi.org/10.1146/annurev.astro.46.060407.145222)
- 1289 Astropy Collaboration, Robitaille, T. P., Tollerud, E. J.,
 1290 et al. 2013, Astronomy & Astrophysics, 558, A33,
 1291 doi: [10.1051/0004-6361/201322068](https://doi.org/10.1051/0004-6361/201322068)
- 1292 Astropy Collaboration, Price-Whelan, A. M., Sipőcz, B. M.,
 1293 et al. 2018, The Astronomical Journal, 156, 123,
 1294 doi: [10.3847/1538-3881/aabc4f](https://doi.org/10.3847/1538-3881/aabc4f)
- 1295 Astropy Collaboration, Price-Whelan, A. M., Lim, P. L.,
 1296 et al. 2022, The Astrophysical Journal, 935, 167,
 1297 doi: [10.3847/1538-4357/ac7c74](https://doi.org/10.3847/1538-4357/ac7c74)
- 1298 Bailer-Jones, C. A. L., Rybizki, J., Fouesneau, M.,
 1299 Demleitner, M., & Andrae, R. 2021, The Astronomical
 1300 Journal, 161, 147, doi: [10.3847/1538-3881/abd806](https://doi.org/10.3847/1538-3881/abd806)
- 1301 Beane, A., Johnson, J., Semenov, V., et al. 2024, Rising
 1302 from the Ashes II: The Bar-driven Abundance
 1303 Bimodality of the Milky Way, arXiv.
 1304 <http://arxiv.org/abs/2410.21580>
- 1305 Belokurov, V., Erkal, D., Evans, N. W., Koposov, S. E., &
 1306 Deason, A. J. 2018, Monthly Notices of the Royal
 1307 Astronomical Society, 478, 611,
 1308 doi: [10.1093/mnras/sty982](https://doi.org/10.1093/mnras/sty982)
- 1309 Bennett, M., & Bovy, J. 2019, Monthly Notices of the
 1310 Royal Astronomical Society, 482, 1417,
 1311 doi: [10.1093/mnras/sty2813](https://doi.org/10.1093/mnras/sty2813)
- 1312 Bensby, T., Feltzing, S., & Oey, M. S. 2014, Astronomy and
 1313 Astrophysics, 562, A71,
 1314 doi: [10.1051/0004-6361/201322631](https://doi.org/10.1051/0004-6361/201322631)
- 1315 Bland-Hawthorn, J., & Gerhard, O. 2016, Annual Review
 1316 of Astronomy and Astrophysics, 54, 529,
 1317 doi: [10.1146/annurev-astro-081915-023441](https://doi.org/10.1146/annurev-astro-081915-023441)
- 1318 Bowen, I. S., & Vaughan, Jr., A. H. 1973, Applied Optics,
 1319 12, 1430, doi: [10.1364/AO.12.001430](https://doi.org/10.1364/AO.12.001430)

- Cao, K., & Pinsonneault, M. H. 2025, Modeling APOKASC-3 red giants: I. The first dredge-up and red giant branch bump, doi: [10.48550/arXiv.2501.14867](https://doi.org/10.48550/arXiv.2501.14867)
- Chen, B., Hayden, M. R., Sharma, S., et al. 2023, Monthly Notices of the Royal Astronomical Society, 523, 3791, doi: [10.1093/mnras/stad1568](https://doi.org/10.1093/mnras/stad1568)
- Chen, T., & Prantzos, N. 2025, Recent star formation episodes in the Galaxy: impact on its chemical properties and the evolution of its abundance gradient, arXiv, doi: [10.48550/arXiv.2501.03342](https://doi.org/10.48550/arXiv.2501.03342)
- Chiappini, C., Matteucci, F., & Gratton, R. 1997, The Astrophysical Journal, 477, 765, doi: [10.1086/303726](https://doi.org/10.1086/303726)
- Chiappini, C., Matteucci, F., & Romano, D. 2001, The Astrophysical Journal, 554, 1044, doi: [10.1086/321427](https://doi.org/10.1086/321427)
- Chiappini, C., Romano, D., & Matteucci, F. 2003, Monthly Notices of the Royal Astronomical Society, 339, 63, doi: [10.1046/j.1365-8711.2003.06154.x](https://doi.org/10.1046/j.1365-8711.2003.06154.x)
- Chieffi, A., & Limongi, M. 2004, The Astrophysical Journal, 608, 405, doi: [10.1086/392523](https://doi.org/10.1086/392523)
- Christensen, C., Quinn, T., Governato, F., et al. 2012, Monthly Notices of the Royal Astronomical Society, 425, 3058, doi: [10.1111/j.1365-2966.2012.21628.x](https://doi.org/10.1111/j.1365-2966.2012.21628.x)
- Conroy, C., Weinberg, D. H., Naidu, R. P., et al. 2022, Birth of the Galactic Disk Revealed by the H3 Survey, doi: [10.48550/arXiv.2204.02989](https://doi.org/10.48550/arXiv.2204.02989)
- Dubay, L. O., Johnson, J. A., & Johnson, J. W. 2024, Galactic Chemical Evolution Models Favor an Extended Type Ia Supernova Delay-Time Distribution, arXiv, doi: [10.48550/arXiv.2404.08059](https://doi.org/10.48550/arXiv.2404.08059)
- Feuillet, D. K., Bovy, J., Holtzman, J., et al. 2018, Monthly Notices of the Royal Astronomical Society, 477, 2326, doi: [10.1093/mnras/sty779](https://doi.org/10.1093/mnras/sty779)
- Frankel, N., Rix, H.-W., Ting, Y.-S., Ness, M., & Hogg, D. W. 2018, The Astrophysical Journal, 865, 96, doi: [10.3847/1538-4357/aadba5](https://doi.org/10.3847/1538-4357/aadba5)
- François, P., Matteucci, F., Cayrel, R., et al. 2004, Astronomy & Astrophysics, 421, 613, doi: [10.1051/0004-6361:20034140](https://doi.org/10.1051/0004-6361:20034140)
- Fuhrmann, K. 1998, Astronomy and Astrophysics, 338, 161, <https://ui.adsabs.harvard.edu/abs/1998A&A...338..161F>
- Fuhrmann, K., Chini, R., Kaderhandt, L., & Chen, Z. 2017, Monthly Notices of the Royal Astronomical Society, 464, 2610, doi: [10.1093/mnras/stw2526](https://doi.org/10.1093/mnras/stw2526)
- Gaia Collaboration, Prusti, T., de Bruijne, J. H. J., et al. 2016, Astronomy and Astrophysics, 595, A1, doi: [10.1051/0004-6361/201629272](https://doi.org/10.1051/0004-6361/201629272)
- Gaia Collaboration, Brown, A. G. A., Vallenari, A., et al. 2021, Astronomy and Astrophysics, 649, A1, doi: [10.1051/0004-6361/202039657](https://doi.org/10.1051/0004-6361/202039657)
- Gallart, C., Bernard, E. J., Brook, C. B., et al. 2019, Nature Astronomy, 3, 932, doi: [10.1038/s41550-019-0829-5](https://doi.org/10.1038/s41550-019-0829-5)
- García Pérez, A. E., Allende Prieto, C., Holtzman, J. A., et al. 2016, The Astronomical Journal, 151, 144, doi: [10.3847/0004-6256/151/6/144](https://doi.org/10.3847/0004-6256/151/6/144)
- Gilmore, G., & Reid, N. 1983, Monthly Notices of the Royal Astronomical Society, 202, 1025, doi: [10.1093/mnras/202.4.1025](https://doi.org/10.1093/mnras/202.4.1025)
- GRAVITY Collaboration, Abuter, R., Amorim, A., et al. 2018, Astronomy and Astrophysics, 615, L15, doi: [10.1051/0004-6361/201833718](https://doi.org/10.1051/0004-6361/201833718)
- Gunn, J. E., Siegmund, W. A., Mannery, E. J., et al. 2006, The Astronomical Journal, 131, 2332, doi: [10.1086/500975](https://doi.org/10.1086/500975)
- Hayden, M. R., Bovy, J., Holtzman, J. A., et al. 2015, The Astrophysical Journal, 808, 132, doi: [10.1088/0004-637X/808/2/132](https://doi.org/10.1088/0004-637X/808/2/132)
- Helmi, A., Babusiaux, C., Koppelman, H. H., et al. 2018, Nature, 563, 85, doi: [10.1038/s41586-018-0625-x](https://doi.org/10.1038/s41586-018-0625-x)
- Holtzman, J. A., Shetrone, M., Johnson, J. A., et al. 2015, The Astronomical Journal, 150, 148, doi: [10.1088/0004-6256/150/5/148](https://doi.org/10.1088/0004-6256/150/5/148)
- Howell, D. A., Sullivan, M., Brown, E. F., et al. 2009, The Astrophysical Journal, 691, 661, doi: [10.1088/0004-637X/691/1/661](https://doi.org/10.1088/0004-637X/691/1/661)
- Hunter, J. D. 2007, Computing in Science & Engineering, 9, 90, doi: [10.1109/MCSE.2007.55](https://doi.org/10.1109/MCSE.2007.55)
- Iwamoto, K., Brachwitz, F., Nomoto, K., et al. 1999, The Astrophysical Journal Supplement Series, 125, 439, doi: [10.1086/313278](https://doi.org/10.1086/313278)
- Johnson, J. W., & Weinberg, D. H. 2020, Monthly Notices of the Royal Astronomical Society, 498, 1364, doi: [10.1093/mnras/staa2431](https://doi.org/10.1093/mnras/staa2431)
- Johnson, J. W., Weinberg, D. H., Vincenzo, F., et al. 2021, Monthly Notices of the Royal Astronomical Society, 508, 4484, doi: [10.1093/mnras/stab2718](https://doi.org/10.1093/mnras/stab2718)
- Johnson, J. W., Weinberg, D. H., Blanc, G. A., et al. 2024, The Milky Way Radial Metallicity Gradient as an Equilibrium Phenomenon: Why Old Stars are Metal-Rich, doi: [10.48550/arXiv.2410.13256](https://doi.org/10.48550/arXiv.2410.13256)
- Jurić, M., Ivezić, , Brooks, A., et al. 2008, The Astrophysical Journal, 673, 864, doi: [10.1086/523619](https://doi.org/10.1086/523619)
- Jönsson, H., Holtzman, J. A., Allende Prieto, C., et al. 2020, The Astronomical Journal, 160, 120, doi: [10.3847/1538-3881/aba592](https://doi.org/10.3847/1538-3881/aba592)
- Kennicutt, Jr., R. C. 1998, The Astrophysical Journal, 498, 541, doi: [10.1086/305588](https://doi.org/10.1086/305588)
- Kubryk, M., Prantzos, N., & Athanassoula, E. 2015, Astronomy and Astrophysics, 580, A126, doi: [10.1051/0004-6361/201424171](https://doi.org/10.1051/0004-6361/201424171)

- Lehmann, C., Feltzing, S., Feuillet, D., & Kordopatis, G. 2024, *Monthly Notices of the Royal Astronomical Society*, 533, 538, doi: [10.1093/mnras/stae1736](https://doi.org/10.1093/mnras/stae1736)
- Leroy, A. K., Walter, F., Brinks, E., et al. 2008, *The Astronomical Journal*, 136, 2782, doi: [10.1088/0004-6256/136/6/2782](https://doi.org/10.1088/0004-6256/136/6/2782)
- Leung, H. W., Bovy, J., Mackereth, J. T., & Miglio, A. 2023, *Monthly Notices of the Royal Astronomical Society*, 522, 4577, doi: [10.1093/mnras/stad1272](https://doi.org/10.1093/mnras/stad1272)
- Licquia, T. C., & Newman, J. A. 2015, *The Astrophysical Journal*, 806, 96, doi: [10.1088/0004-637X/806/1/96](https://doi.org/10.1088/0004-637X/806/1/96)
- Limongi, M., & Chieffi, A. 2006, *The Astrophysical Journal*, 647, 483, doi: [10.1086/505164](https://doi.org/10.1086/505164)
- Lu, Y. L., Minchev, I., Buck, T., et al. 2024, *Monthly Notices of the Royal Astronomical Society*, 535, 392, doi: [10.1093/mnras/stae2364](https://doi.org/10.1093/mnras/stae2364)
- Mackereth, J. T., Crain, R. A., Schiavon, R. P., et al. 2018, *Monthly Notices of the Royal Astronomical Society*, 477, 5072, doi: [10.1093/mnras/sty972](https://doi.org/10.1093/mnras/sty972)
- Mackereth, J. T., Bovy, J., Schiavon, R. P., et al. 2017, *Monthly Notices of the Royal Astronomical Society*, 471, 3057, doi: [10.1093/mnras/stx1774](https://doi.org/10.1093/mnras/stx1774)
- Mackereth, J. T., Bovy, J., Leung, H. W., et al. 2019, *Monthly Notices of the Royal Astronomical Society*, 489, 176, doi: [10.1093/mnras/stz1521](https://doi.org/10.1093/mnras/stz1521)
- Majewski, S. R., Schiavon, R. P., Frinchaboy, P. M., et al. 2017, *The Astronomical Journal*, 154, 94, doi: [10.3847/1538-3881/aa784d](https://doi.org/10.3847/1538-3881/aa784d)
- Maoz, D., & Graur, O. 2017, *The Astrophysical Journal*, 848, 25, doi: [10.3847/1538-4357/aa8b6e](https://doi.org/10.3847/1538-4357/aa8b6e)
- Maoz, D., & Mannucci, F. 2012, *Publications of the Astronomical Society of Australia*, 29, 447, doi: [10.1071/AS11052](https://doi.org/10.1071/AS11052)
- Matteucci, F., & Greggio, L. 1986, *Astronomy and Astrophysics*, 154, 279. <https://ui.adsabs.harvard.edu/abs/1986A&A...154..279M/abstract>
- Matteucci, F., Spitoni, E., Recchi, S., & Valiante, R. 2009, *Astronomy and Astrophysics*, 501, 531, doi: [10.1051/0004-6361/200911869](https://doi.org/10.1051/0004-6361/200911869)
- Mazzali, P. A., Röpke, F. K., Benetti, S., & Hillebrandt, W. 2007, *Science*, 315, 825, doi: [10.1126/science.1136259](https://doi.org/10.1126/science.1136259)
- Melioli, C., Brighenti, F., D’Ercole, A., & de Gouveia Dal Pino, E. M. 2008, *Monthly Notices of the Royal Astronomical Society*, 388, 573, doi: [10.1111/j.1365-2966.2008.13446.x](https://doi.org/10.1111/j.1365-2966.2008.13446.x)
- . 2009, *Monthly Notices of the Royal Astronomical Society*, 399, 1089, doi: [10.1111/j.1365-2966.2009.14725.x](https://doi.org/10.1111/j.1365-2966.2009.14725.x)
- Naidu, R. P., Conroy, C., Bonaca, A., et al. 2021, *The Astrophysical Journal*, 923, 92, doi: [10.3847/1538-4357/ac2d2d](https://doi.org/10.3847/1538-4357/ac2d2d)
- Nataf, D. M., Schlaufman, K. C., Reggiani, H., & Hahn, I. 2024, *Accurate, Precise, and Physically Self-consistent Ages and Metallicities for 400,000 Solar Neighborhood Subgiant Branch Stars*, arXiv, doi: [10.48550/arXiv.2407.18307](https://doi.org/10.48550/arXiv.2407.18307)
- Nidever, D. L., Holtzman, J. A., Allende Prieto, C., et al. 2015, *The Astronomical Journal*, 150, 173, doi: [10.1088/0004-6256/150/6/173](https://doi.org/10.1088/0004-6256/150/6/173)
- Nissen, P. E., Christensen-Dalsgaard, J., Mosumgaard, J. R., et al. 2020, *Astronomy and Astrophysics*, 640, A81, doi: [10.1051/0004-6361/202038300](https://doi.org/10.1051/0004-6361/202038300)
- Palicio, P. A., Spitoni, E., Recio-Blanco, A., et al. 2023, *Analytic solution of Chemical Evolution Models with Type Ia SNe*, arXiv, doi: [10.48550/arXiv.2304.00042](https://doi.org/10.48550/arXiv.2304.00042)
- Palla, M., Magrini, L., Spitoni, E., et al. 2024, *Astronomy & Astrophysics*, 690, A334, doi: [10.1051/0004-6361/202451395](https://doi.org/10.1051/0004-6361/202451395)
- Palla, M., Matteucci, F., Spitoni, E., Vincenzo, F., & Grisoni, V. 2020, *Monthly Notices of the Royal Astronomical Society*, 498, 1710, doi: [10.1093/mnras/staa2437](https://doi.org/10.1093/mnras/staa2437)
- Palla, M., Santos-Peral, P., Recio-Blanco, A., & Matteucci, F. 2022, *Astronomy and Astrophysics*, 663, A125, doi: [10.1051/0004-6361/202142645](https://doi.org/10.1051/0004-6361/202142645)
- Parul, H., Bailin, J., Loebman, S. R., et al. 2025, *Effect of gas accretion on α -element bimodality in Milky Way-mass galaxies in the FIRE-2 simulations*, arXiv, doi: [10.48550/arXiv.2501.12342](https://doi.org/10.48550/arXiv.2501.12342)
- Pedregosa, F., Varoquaux, G., Gramfort, A., et al. 2011, *Journal of Machine Learning Research*, 12, 2825. <http://jmlr.org/papers/v12/pedregosa11a.html>
- Pinsonneault, M. H., Zinn, J. C., Tayar, J., et al. 2025, *The Astrophysical Journal Supplement Series*, 276, 69, doi: [10.3847/1538-4365/ad9fef](https://doi.org/10.3847/1538-4365/ad9fef)
- Prantzos, N., Abia, C., Chen, T., et al. 2023, *Monthly Notices of the Royal Astronomical Society*, 523, 2126, doi: [10.1093/mnras/stad1551](https://doi.org/10.1093/mnras/stad1551)
- Ratcliffe, B., Minchev, I., Anders, F., et al. 2023, *Monthly Notices of the Royal Astronomical Society*, 525, 2208, doi: [10.1093/mnras/stad1573](https://doi.org/10.1093/mnras/stad1573)
- Rodríguez, , Maoz, D., & Nakar, E. 2023, *The Astrophysical Journal*, 955, 71, doi: [10.3847/1538-4357/ace2bd](https://doi.org/10.3847/1538-4357/ace2bd)
- Romano, D., Matteucci, F., Salucci, P., & Chiappini, C. 2000, *The Astrophysical Journal*, 539, 235, doi: [10.1086/309223](https://doi.org/10.1086/309223)
- Ruiz-Lara, T., Gallart, C., Bernard, E. J., & Cassisi, S. 2020, *Nature Astronomy*, 4, 965, doi: [10.1038/s41550-020-1097-0](https://doi.org/10.1038/s41550-020-1097-0)

- Schönrich, R., & Binney, J. 2009, *Monthly Notices of the Royal Astronomical Society*, 396, 203, doi: [10.1111/j.1365-2966.2009.14750.x](https://doi.org/10.1111/j.1365-2966.2009.14750.x)
- Sellwood, J. A., & Binney, J. J. 2002, *Monthly Notices of the Royal Astronomical Society*, 336, 785, doi: [10.1046/j.1365-8711.2002.05806.x](https://doi.org/10.1046/j.1365-8711.2002.05806.x)
- Sharma, S., Hayden, M. R., & Bland-Hawthorn, J. 2021, *Monthly Notices of the Royal Astronomical Society*, 507, 5882, doi: [10.1093/mnras/stab2015](https://doi.org/10.1093/mnras/stab2015)
- Siegel, M. H., Majewski, S. R., Reid, I. N., & Thompson, I. B. 2002, *The Astrophysical Journal*, 578, 151, doi: [10.1086/342469](https://doi.org/10.1086/342469)
- Spitoni, E., Cescutti, G., Minchev, I., et al. 2019, *Astronomy and Astrophysics*, 628, A38, doi: [10.1051/0004-6361/201834665](https://doi.org/10.1051/0004-6361/201834665)
- Spitoni, E., & Matteucci, F. 2011, *Astronomy and Astrophysics*, 531, A72, doi: [10.1051/0004-6361/201015749](https://doi.org/10.1051/0004-6361/201015749)
- Spitoni, E., Matteucci, F., Gratton, R., et al. 2024, *Astronomy & Astrophysics*, 690, A208, doi: [10.1051/0004-6361/202450754](https://doi.org/10.1051/0004-6361/202450754)
- Spitoni, E., Matteucci, F., Recchi, S., Cescutti, G., & Pipino, A. 2009, *Astronomy and Astrophysics*, 504, 87, doi: [10.1051/0004-6361/200911768](https://doi.org/10.1051/0004-6361/200911768)
- Spitoni, E., Recchi, S., & Matteucci, F. 2008, *Astronomy and Astrophysics*, 484, 743, doi: [10.1051/0004-6361:200809403](https://doi.org/10.1051/0004-6361:200809403)
- Spitoni, E., Romano, D., Matteucci, F., & Ciotti, L. 2015, *The Astrophysical Journal*, 802, 129, doi: [10.1088/0004-637X/802/2/129](https://doi.org/10.1088/0004-637X/802/2/129)
- Spitoni, E., Verma, K., Silva Aguirre, V., & Calura, F. 2020, *Astronomy and Astrophysics*, 635, A58, doi: [10.1051/0004-6361/201937275](https://doi.org/10.1051/0004-6361/201937275)
- Spitoni, E., Verma, K., Silva Aguirre, V., et al. 2021, *Astronomy and Astrophysics*, 647, A73, doi: [10.1051/0004-6361/202039864](https://doi.org/10.1051/0004-6361/202039864)
- Spitoni, E., Recio-Blanco, A., de Laverny, P., et al. 2023, *Astronomy and Astrophysics*, 670, A109, doi: [10.1051/0004-6361/202244349](https://doi.org/10.1051/0004-6361/202244349)
- Sukhbold, T., Ertl, T., Woosley, S. E., Brown, J. M., & Janka, H. T. 2016, *The Astrophysical Journal*, 821, 38, doi: [10.3847/0004-637X/821/1/38](https://doi.org/10.3847/0004-637X/821/1/38)
- Sánchez, S. F. 2020, *Annual Review of Astronomy and Astrophysics*, 58, 99, doi: [10.1146/annurev-astro-012120-013326](https://doi.org/10.1146/annurev-astro-012120-013326)
- Tinsley, B. M. 1979, *The Astrophysical Journal*, 229, 1046, doi: [10.1086/157039](https://doi.org/10.1086/157039)
- Virtanen, P., Gommers, R., Oliphant, T. E., et al. 2020, *Nature Methods*, 17, 261, doi: [10.1038/s41592-019-0686-2](https://doi.org/10.1038/s41592-019-0686-2)
- Weinberg, D. H., Andrews, B. H., & Freudenburg, J. 2017, *The Astrophysical Journal*, 837, 183, doi: [10.3847/1538-4357/837/2/183](https://doi.org/10.3847/1538-4357/837/2/183)
- Weinberg, D. H., Griffith, E. J., Johnson, J. W., & Thompson, T. A. 2024, *The Astrophysical Journal*, 973, 122, doi: [10.3847/1538-4357/ad6313](https://doi.org/10.3847/1538-4357/ad6313)
- Wilson, J. C., Hearty, F. R., Skrutskie, M. F., et al. 2019, *Publications of the Astronomical Society of the Pacific*, 131, 055001, doi: [10.1088/1538-3873/ab0075](https://doi.org/10.1088/1538-3873/ab0075)
- Woody, T., Conroy, C., Cargile, P., et al. 2025, *The Astrophysical Journal*, 978, 152, doi: [10.3847/1538-4357/ad968e](https://doi.org/10.3847/1538-4357/ad968e)
- Woosley, S. E., & Weaver, T. A. 1995, *The Astrophysical Journal Supplement Series*, 101, 181, doi: [10.1086/192237](https://doi.org/10.1086/192237)